

# 1 Chemical sparsity in Bayesian receptor models for aerosol 2 source apportionment

3 Marta Via<sup>1</sup>, Jure Demšar<sup>2</sup>, Yufang Hao<sup>3</sup>, Manousos Manousakas<sup>3,4</sup>, Anton Rusanen<sup>5</sup>, Jianhui  
4 Jiang<sup>6</sup>, Stuart K. Grange<sup>7</sup>, Jean-Luc Jaffrezo<sup>8</sup>, Vy Ngoc Thuy Dinh<sup>8</sup>, Gaëlle Uzu<sup>8</sup>, Griša  
5 Močnik<sup>1</sup>, and Kaspar R. Daellenbach<sup>3</sup>

6  
7 <sup>1</sup>Center for Atmospheric Research, University of Nova Gorica, Ajdovščina 5270, Slovenia

8 <sup>2</sup>Faculty of Computer and Information Science, Tržaška Cesta 25, 1000 Ljubljana, Slovenia

9 <sup>3</sup>Laboratory of Atmospheric Chemistry, Paul Scherrer Institute, 5232 Villigen PSI, Switzerland

10 <sup>4</sup>Environmental Radioactivity Aerosol Tech. for Atmospheric Climate Impacts, INRaSTES, National Centre of  
11 Scientific Research “Demokritos”, Ag. Paraskevi, 15310, Greece

12 <sup>5</sup>Atmospheric Composition Research, Finnish Meteorological Institute, 00101 Helsinki, Finland

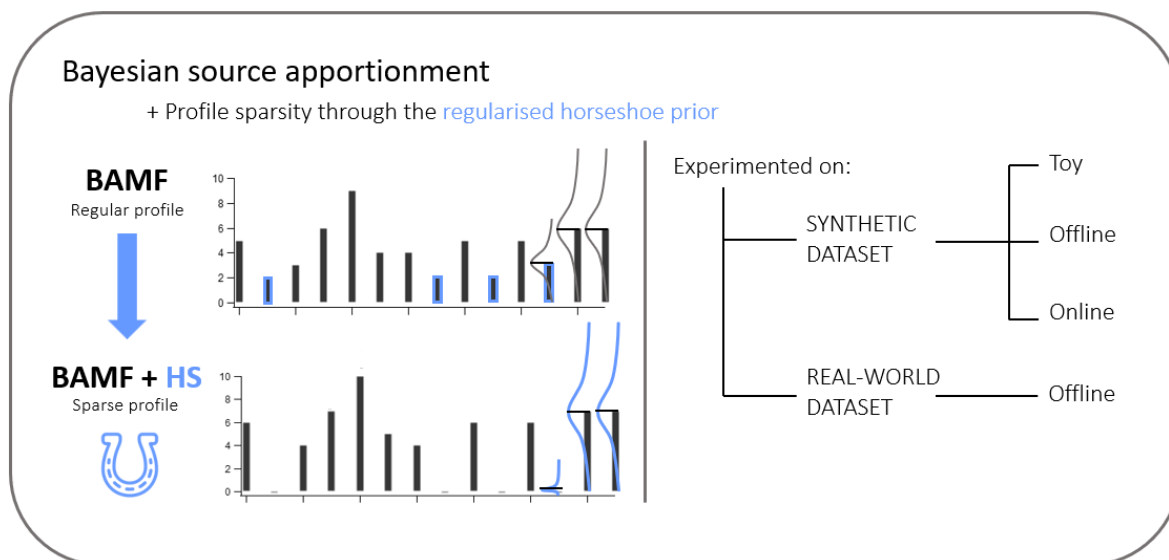
13 <sup>6</sup>School of Ecological and Environmental Sciences, East China Normal University, 200241, Shanghai, China

14 <sup>7</sup>Climate and Environmental Physics, Physics Institute, University of Bern, Sidlerstrasse 5, 3012 Bern,  
15 Switzerland

16 <sup>8</sup>University of Grenoble Alpes, CNRS, INRAE, IRD, Grenoble INP, IGE, Grenoble 38000, France

17  
18 *Correspondence to:* Marta Via ([marta.viagonzalez@ung.si](mailto:marta.viagonzalez@ung.si)) and Kaspar R. Daellenbach  
19 ([kaspar.daellenbach@psi.ch](mailto:kaspar.daellenbach@psi.ch))

20 **Abstract.** Aerosol source apportionment is a key tool for understanding the origins of atmospheric particulate  
21 matter and for guiding effective air quality management strategies. However, source apportionment techniques  
22 still struggle to properly separate highly correlated sources without relying on restrictive *a priori* information,  
23 possibly skewing the solution and adding subjective operator input, with varying degrees of benefit. This study  
24 introduces sparsity into the Bayesian Autocorrelated Matrix Factorisation (BAMF) model with the aim of  
25 removing non-essential species contribution in the unconstrained profiles, which is expected to improve the  
26 separation of factors compared to BAMF. The regularised horseshoe prior (HS) has been added to BAMF  
27 (BAMF+HS) to promote composition matrix  $\mathbf{F}$  sparsity, shrinking low-signal contributions to the solutions.  
28 BAMF+HS was evaluated using three synthetic datasets designed to reflect increasing levels of data complexity  
29 (Toy, representing a highly simplified dataset; Offline, representing a filter dataset; and Online, representing an  
30 Aerosol Chemical Speciation Monitor (ACSM)-like dataset), and a real-world multi-site filter dataset. The results  
31 demonstrate that BAMF+HS effectively enforces sparsity in offline datasets and that this improves accuracy in  
32 reconstructing source profiles and time series compared to BAMF and Positive Matrix Factorisation (PMF).  
33 However, its application to higher-complexity ACSM datasets revealed sensitivity to sampling instability  
34 hindering sparsification. With that, even though sparsity was not achieved, the quality of the BAMF+HS solution  
35 metrics were not deprecated compared to BAMF. Overall, this work underscores the value of incorporating profile  
36 sparsity as a solution property in Bayesian source apportionment, and positions BAMF+HS as a promising model  
37 for source apportionment.



39

## 40 1. Introduction

41 Particulate Matter (PM) adversely affects human health through both short and sustained exposures (Pope and  
42 Dockerty, 1999, Yang et al. 2019). The observed relationship between decreasing PM concentrations and  
43 increased life expectancy (Keuken et al. 2011; Zheng et al. 2022) highlights the importance of developing  
44 mitigation plans grounded in detailed knowledge of PM sources composition and concentrations. Moreover,  
45 because some proxies for aerosol toxicity, among them oxidative potential, are highly dependent on its sources  
46 (Daellenbach et al. 2020), implementing source-specific mitigation measures contributes to more quantitative and  
47 efficient abatement and a more effective protection of the population.

48

49 Source apportionment is the process of identifying and quantifying sources by using information about their  
50 chemical composition, and is commonly conducted through receptor models (RMs) which differentiate PM  
51 sources according to the distinctness of their chemical composition and time series characteristics. The most  
52 widely used RM is the Positive Matrix Factorisation model (PMF, Paatero and Tapper, 1994), which deconvolutes  
53 the input chemical composition into the product of composition and time series matrices ( $\mathbf{F}$  and  $\mathbf{G}$ , respectively),  
54 and minimises the residuals of the fit through the weighted least squares loss. The factorisation equation, hence,  
55 is written as

$$56 \quad \mathbf{X} = \mathbf{G} \cdot \mathbf{F} + \mathbf{E}, \quad (1)$$

57 where  $\mathbf{X}$  is the input matrix, a  $n \cdot m$  matrix of  $n$  timepoints and  $m$  species, which is decomposed into  $\mathbf{G}$  and  $\mathbf{F}$ ,  
58 matrices of dimensions  $n \cdot p$  and  $p \cdot m$ , respectively, where  $p$  is the number of factors, and  $\mathbf{E}$  is the residuals matrix  
59 of dimensions  $n \cdot m$ .

60

61 Unconstrained PMF, although it can lead to robust results, is usually insufficient when the sources are highly  
62 correlated or have very similar source profiles. In such cases, guiding the model by introducing a priori knowledge  
63 (common practice known as constraining the model) has been proven beneficial for the source deconvolution  
64 (Lingwall and Christensen et al. 2007, Belis et al. 2014, Dinh et al. 2025). However, it can still introduce

65 substantial bias in the solution (Via et al. 2022). Globally, the RMs cover the whole range of pollution sources  
66 knowledge required prior to receptor modelling (Viana et al. 2008, Belis et al. 2013). A very strongly-constrained  
67 RM is the Chemical Mass Balance model (CMB), which factorises the initial matrices with a totally fixed  $\mathbf{G}$  or  $\mathbf{F}$ .

68  
69 Bayesian models represent a probabilistic alternative to the PMF framework. The first application of Bayesian  
70 models in atmospheric source apportionment was introduced in Park et al. (2001, 2002) for Volatile Organic  
71 Compounds (VOC) source apportionment. In this approach, the mass closure condition was taken to the Bayesian  
72 framework and an autocorrelation prior AR(1) (the first order autoregression) was applied, improving the solution  
73 given assuming independent  $\mathbf{G}$  components. The autocorrelation prior importance was later reinforced in Rusanen  
74 et al. (2024) with a differently formulated autocorrelation prior. The latter shows the added value of the Bayesian  
75 Autocorrelated Matrix Factorisation model (BAMF) in comparison to PMF in different kinds of spectrometry-  
76 based PM synthetic datasets. The Bayesian Multivariate receptor modelling software BNFA and bayesMRM (Park  
77 and Oh, 2021) were developed to provide user-friendly tools for Bayesian source apportionment.

78  
79 However, studies using the Bayesian Matrix Factorisation framework are still scarce. Some examples are Oh and  
80 Park (2022), which employed a Bayesian RM to conduct multi-site source apportionment, and Zhang et al. (2023),  
81 which performed  $\text{NH}_4^+$  source apportionment through the Bayesian SIMMR package (Govan et al. 2023).  
82 Bayesian models have also been used as a complement to standard RMs, as in Balachandran et al. (2013) where  
83 a Bayesian model processing ensemble solutions of a chemical transport model and solutions of three RMs are  
84 produced to then use it in CMB for production of final results. The Bayesian model focused on attributing the  
85 proper weight to each of the ensemble components and improved the correlation of sources with their markers  
86 compared to the traditional approach. Bayesian inference has also been used in Park et al. (2002) and Dai et al.  
87 (2024) to generate spatially resolved source apportionment solutions adjusting the weights of each location  
88 solution in a multi-site data scheme.

89  
90 Thus, Bayesian Matrix Factorisation has become an effective and powerful tool for aerosol source apportionment.  
91 However, to the authors knowledge, little attention has been given to improving the accuracy of chemical  
92 composition profiles, i.e.  $\mathbf{F}$  components. This highlights the fundamental challenge in receptor modelling of  
93 obtaining chemically distinct and interpretable source profiles from complex and mixed emission sources.  
94 Moreover, it has been shown in Rusanen et al. (2024) that in BAMF, slight differences of  $\mathbf{F}$  can severely  
95 compromise the quality of  $\mathbf{G}$  (Figure S2 in the mentioned article), hence, steps towards  $\mathbf{F}$  refining should result  
96 in overall source apportionment method improvement. In this context, sparsity, defined as the property of a  
97 dataset, model or solution in which only a limited number of elements are substantial contributions while most  
98 are zero or close to zero, could be favourable for this problem. The accomplishment of sparse source fingerprints  
99 could represent “cleaner” emission sources with less mixing among resolved factor profiles, since substituting  
100 non-significant contributions in a factor by zeros might allow allocating more importance to the actually relevant  
101 contributions of species in factors. This work aims to implement sparsity on chemical fingerprints in BAMF  
102 aiming for a more accurate source apportionment. We introduce sparsity with the regularised horseshoe prior  
103 (Piiroinen and Vehtari, 2017), which unlike other sparsity priors, enables regularisation of the sparsity strength,  
104 and compare it with other sparsity priors, such as Lasso (Tibshirani et al. 2015) and Spike-and-slab (Andersen et

105 al. 2014). This model is then tested on three synthetic datasets with different complexity degrees and one real-  
106 world dataset to depict the impact of sparsity and potential benefits of its implementation.

## 107 2. Methodology

### 108 2.1 Bayesian Matrix Factorisation

109

110 Bayesian Matrix factorisation models, like other RMs, are based on the chemical mass balance equation (Eq. 1).  
111 Bayesian modeling approaches this problem probabilistically and bases the determination of the matrices,  $\mathbf{F}$  and  
112  $\mathbf{G}$ , the main parameters to determine, upon the assumptions imposed on the model, i.e. priors. Bayesian  
113 factorisation forces the decomposition through modelling the  $\mathbf{X}$  matrix components as a Gaussian with center on  
114 the “noise-free data matrix”  $\mathbf{Z}$  (matrix of dimensions  $n \cdot m$ ) and a standard deviation given by the positively-defined  
115 uncertainty matrix (Eq. 2). The matrix  $\sigma$  (positive matrix of dimensions  $n \cdot m$ ) represents the uncertainties of the  
116 measurements. The matrix  $\mathbf{Z}$  is, in turn, the product of the time series and profiles submatrices,  $\mathbf{G}$  and  $\mathbf{F}$ ,  
117 respectively, and (a) is rewritten as:

$$118 \quad X \sim N(\mathbf{Z}, \sigma) = N(\mathbf{G} \cdot \mathbf{F}, \sigma) \quad (2)$$

119 where  $N$  represents the normal distribution. Whilst  $\mathbf{G}$  is not given any prior and is sampled then by default from  
120 a uniform distribution,  $\mathbf{F}$  is modelled as a Dirichlet distribution to ensure positivity, with the sum of its components  
121 being equal to 1 (2):

$$122 \quad F_k \sim \text{Dirichlet}(1_m) \quad (3)$$

123 With these  $\mathbf{F}$  requirements, profiles represent the normalised contribution to the spectra of one source. Usual  
124 notation for indices used hereinafter are  $i, j, k$  for elements in the range  $(1, \dots, n)$ ,  $(1, \dots, m)$ , and  $(1, \dots, p)$ , for the  
125 timestamps, species, and factors, respectively. It is worth noting that PMF applies the normalisation of profiles  
126 after a  $\mathbf{F}$ ,  $\mathbf{G}$  solution is found, not as a model prior as done in BAMF. The PMF generates mass-loaded  $\mathbf{F}$ ,  $\mathbf{G}$   
127 solution matrices, which are reweighted to provide a normalised  $\mathbf{F}$  and a mass-loaded  $\mathbf{G}$ . In the Bayesian models  
128 used in this study, the normalisation of  $\mathbf{F}$  is inherent to the model by design. The different formulations eventually  
129 provide normalised  $\mathbf{F}$  and mass-weighted  $\mathbf{G}$ , with unlikely affectations due to the normalisation procedure. The  
130 model configuration given by (2) and (3) will be referred to as Bayesian Factorisation model (BMF) and represents  
131 the analog of PMF in the Bayesian framework. All models used in this manuscript are outlined in Table 1.

132 On top of this structure, Rusanen et al (2024) proposed an autocorrelation prior for  $\mathbf{G}$  which should account for  
133 the inherent autocorrelation of air pollutant sources in time. The formulation of the autocorrelation prior for  $\mathbf{G}$  is  
134 given by (4) and includes two more modelling parameters,  $\alpha$  (positive vector or dimension  $p$ ) and  $\beta$  (positive  
135 vector or dimension  $p$ ), which regulate the similarity of one  $\mathbf{G}$  component with the previous one as follows:

$$136 \quad G_{i+1,k} \sim C^+(G_{ik}, \alpha_k \cdot \Delta t_i + \beta_k) \quad (4)$$

137 where  $i \in (2, \dots, n-1)$ ,  $C$  represents the Cauchy distribution and  $+$  represents positive real numbers. This prior  
138 centers the  $i+1$ th component distribution in the  $i$ th component with a distribution width that linearly depends on  
139 the temporal gap between these two timestamps. Hence, the more temporally-separated two consecutive points  
140 are, the less correlated they are expected to be. The Cauchy distribution was chosen due to its heavier tails which  
141 enable more probable jumps between consecutive  $i$ 's than a Gaussian distribution (Gelman et al., 2013). This  
142 flexibility could be convenient for real-world datasets which are affected by measurement gaps. The coefficients

143  $\alpha$  and  $\beta$  are source dependent to allow for source-dependent correlation degrees. The model which introduces this  
 144 prior to BMF is called Bayesian Autocorrelation Matrix Factorisation model (BAMF, Rusanen et al. 2024).

### 145 2.1.1 The horseshoe prior

146 The introduction of sparsity in BAMF involves the addition of several hyperpriors in the  $\mathbf{F}$  prior to implement the  
 147 shrinkage mechanism. In this study, we used the regularised horseshoe prior (Piironen and Vehtari, 2017), which  
 148 is a global-local complex of hyperpriors, i.e. the shrinkage power is both regulated globally source-wise and  $\mathbf{F}$ -  
 149 component-wise. The idea behind this prior is that species with very small contributions to a factor are shrunk  
 150 toward zero through an automatic shrinkage mechanism, whereas species with substantial support from the data  
 151 are largely unaffected. The regularised horseshoe (HS) prior implemented in  $\mathbf{F}$  in the BAMF scheme as

$$152 F_{kj} = \mu_{kj} \cdot \tilde{\lambda}_{kj} \cdot \tau_j, \quad (5)$$

153 where  $\mu$  (matrix of dimensions  $n \cdot m$ ) represents the  $\mathbf{F}$  matrix without the horseshoe prior.  $\mu$ , in turn is defined as  
 154 a standard Cauchy distribution prior as

$$155 \mu_{kj} \sim C^+(0, 1), \quad (6)$$

156 where  $\tau$  (vector of dimension  $p$ ) represents the global shrinkage parameters and

$$157 \tau \sim C^+(0, \tau_0 \cdot \sigma_{HS}), \quad (7)$$

158 where the parameter  $\tau_0$  can be regulated by the user to regulate the overall shrinkage power and  $\sigma_{HS}$  is sampled  
 159 from an uniform distribution. The hyperparameter  $\tilde{\lambda}_{kj}$  applies the local shrinkage to

160 as

$$161 \tilde{\lambda}_{kj} = \sqrt{\frac{c^2 \cdot \lambda^2}{c^2 + \lambda^2 \cdot \tau^2}}, \quad (8)$$

162 where

$$163 c^2 \sim \Gamma^{-1}(0.5 \cdot \text{slab\_df}, 0.5 \cdot \text{slab\_df}) \quad (9)$$

$$164 \lambda \sim \text{slab\_scale} \cdot C^+(0, 1) \quad (10)$$

165 both combined providing the characteristic shrinking horseshoe shape. Here,  $\lambda$  is a model parameter of dimensions  
 166  $n \cdot m$  which after regularisation becomes is denoted as  $\tilde{\lambda}$ . Further description of the horseshoe implementation on  
 167 BAMF can be found in Section S2.1, and the prior derivation and details in Piironen and Vehtari (2018). The  
 168 distribution parameters  $\tau_0$ ,  $\sigma_{HS}$ , and  $\text{slab\_df}$ ,  $\text{slab\_scale}$  were tested and results did not show significant sensitivity  
 169 to their variations, so we keep the defaults as provided in Piironen and Vehtari (2018) as can be found in the  
 170 available shared codes. The models with the horseshoe (HS) priors are hereinafter marked with "+HS". Figure S1  
 171 shows a schematic diagram of the matrix decomposition through BAMF.

172

173 In order to assess the amount of sparsity of a dataset or a solution, we used the Gini coefficient (Gini et al., 1936),  
 174 which assesses the inequality over a distribution as follows:

$$175 \text{Gini} = \frac{\sum_{i=1}^n (2 \cdot i - n - 1) \cdot x_i}{2 \cdot n \cdot \sum_{i=1}^n x_i} \quad (11)$$

176 where  $x$  values are sorted in ascending order, and  $n$  is the number of elements in  $x$ . Since it quantifies the  
 177 inequality, it can be a proxy for sparsity; if some values are high and the others are zero,  $\text{Gini} \approx 1$ , if all values are  
 178 equal,  $\text{Gini} = 0$ . Also, the solution-to-truth Gini values ratio will be discussed throughout the analysis, referred to  
 179 as "Gini ratio". To evaluate if the sparsity is enforced precisely where it should, an additional metric has been

180 applied called “zero truth sum”. This metric sums up the modelled contributions of the null species in the truth  
181 profiles.

### 182 2.1.2 Alternative factorisation methodologies

183 **BAMF-AR1.** There is an alternative formulation for the autocorrelation prior as introduced in Bayesian models  
184 by Park et al. (2001). The AR(1) autocorrelation prior is the first degree polynomial expansion of the  
185 autoregressive models and it proposes a linear progression of  $G_{i+1,k}$  from  $G_{i,k}$ . We introduce AR(1) in the Bayesian  
186 framework as

$$187 G_{i+1,k} \sim N(\alpha_k \cdot G_{i,k} + \beta_k, \gamma_k) \quad (12)$$

188 In this formulation, the  $i+1$ -th point stems from a Gaussian distribution centered linear combination on the  $i$ -th  
189 point with source-dependent slopes ( $\alpha$ ) and intercept ( $\beta$ ), and width ( $\gamma$ ). Although, unlike (4), it disregards the  
190 decrease of correlation between gapped consecutive points, this prior allows for source-specific time series trends,  
191 which would be beneficial for certain source description. The model which introduces this prior to BMF will be  
192 called BAMF-AR1.

193

194 **BAMF-GS.** Another formulation is introduced, switching the Dirichlet distribution to the matrix  $\mathbf{G}$  instead of  $\mathbf{F}$   
195 (6). This swap should allow  $\mathbf{F}$  to retain the  $\mathbf{X}$  matrix mass and could potentially help deconvoluting profiles due  
196 to the upweighting of the chemical profiles.

$$197 G_k \sim \text{Dirichlet}(1_n) \quad (13)$$

198 Thus, the  $\mathbf{G}$  presents two priors, the dirichlet distribution and the autocorrelation prior, whilst  $\mathbf{F}$  is sampled from  
199 the default uniform distribution. This model will be called hereinafter BAMF-GS as short from BAMF-G simplex,  
200 since a simplex is the set of positive vectors that sum to one hence it is the natural geometric structure for the  
201 Dirichlet distribution to sit on. This model structure, nevertheless, does not allow for a horseshoe prior application,  
202 since due to the factors mass now incorporated in  $\mathbf{F}$ , the coefficients will be very distinct from zero and the  
203 horseshoe prior will not perceive them as potential signals to sparsify.

204

205 **CMB.** Lastly, a Bayesian formulation of the CMB model was employed in order to test the horseshoe prior  
206 capacities with the most proper factorisation possible. This model is mainly analogous to CMB in the Bayesian  
207 framework, but the  $\mathbf{G}$  matrix was fixed with the truth time series. Hence the model only had to determine the  $\mathbf{F}$   
208 components distributions to match the factorisation condition (2) given the truth  $\mathbf{G}$ .

### 209 2.1.3 Solver and Hamiltonian-Monte Carlo Markov Chain

210 All Bayesian models were compiled and run in STAN (Carpenter et al. 2017), a probabilistic programming  
211 language developed for Bayesian modelling. STAN solves Bayesian inference through the Hamiltonian Monte  
212 Carlo (HMC) algorithm based on Markov Chain Monte Carlo methods (MCMC). HMC uses an approximate  
213 Hamiltonian dynamics simulation with the Metropolis acceptance/rejection criterion and a no-U-turn sampler  
214 (NUTS, Hoffman and Gelman, 2014). For the sake of brevity, we present only the essential concepts here,  
215 directing readers to Carpenter et al. (2017), Gelman et al. (2014), STAN Manual (2025) and references therein for  
216 comprehensive information.

217 The parameters of the model, primarily **F** and **G** but also all the other defined parameters ( $\tau, \lambda, \alpha, \beta$ ) are sampled  
218 from their posterior distributions, constructed from the priors and the data introduced. In the Hamiltonian analogy,  
219 the evolution of these parameters across samples is computed as the trajectory of a fictitious particle. This particle  
220 moves through the parameter space driven by random momentum in all directions. This approach avoids the  
221 random-walk behavior of simpler sampling methods and enables faster convergence. The trajectory is hence  
222 simulated using a discretized approximation, and candidate positions are accepted or rejected according to the  
223 Metropolis criterion (Metropolis et al. 1953). Accepted positions correspond to plausible parameter values given  
224 both the model assumptions and the data. This process provides a distribution over samples of possible solutions  
225 from which confidence intervals of each of the model (hyper)parameters can be extracted. A set of samples is  
226 called a chain, each of them initialised with a different seed to explore the solution space more broadly. In order  
227 to initialise the model parameters more effectively, the maximum a posteriori (MAP) point parameters solution  
228 estimated by STAN is used through the LBFGS algorithm (Liu and Nocedal, 1989). Even if this approach makes  
229 the parameter sampling process much more efficient, solutions might have multiple local maxima, and MAP will  
230 initialise the models based only on one of those. This highlights the importance of using different seeds to explore  
231 the solution space more widely. Since the early iterations of each Markov chain are typically influenced by the  
232 starting values and may not represent samples from the true posterior distribution, we discarded the first half of  
233 the samples from each chain. Different settings were used according to the type of experiment, shown in Table  
234 S1. The number of chains is consistent with standard practice in Bayesian modeling, and the number of samples  
235 was increased beyond commonly adopted values (e.g., 1000) in order to improve solution stability. As seen in  
236 Table S1, the more complex the datasets are, the more time BAMF+HS takes to run. Since the BAMF+HS running  
237 times are high at this development stage, BAMF+HS might currently be more adequate for exhaustive source  
238 apportionment refinement than real-time monitoring.

239 In order to evaluate the convergence of a solution to the target posterior distribution, the potential scale reduction  
240 factor ( $\hat{R}$ , Gelman and Rubin, 1992) is used. This coefficient compares the variance within chains and between  
241 chains of the Z matrix, hence if chains converge,  $\hat{R} \approx 1$ , values of  $\hat{R} \gg 1$  imply chain divergence and values of  $\hat{R} \ll 1$   
242 imply sampling divergence in chains. The convergence of all runs has been assessed using standard Bayesian  
243 diagnostics, including visual inspection of trace plots, and the effective sample size and  $\hat{R}$  statistics, and all  
244 experiments shown in the manuscript fall within satisfactory stability ranges for these criteria.

245

## 246 **2.2 PMF**

247 In PMF (Paatero and Tapper, 1994), equation (1) is solved through the ME-2 solver (ME2, Paatero, 1999) based  
248 on the weighted means squares minimization of the quantity:

$$249 \quad Q = \sum_{j=1}^m \sum_{i=1}^n \left( \frac{e_{ij}}{\sigma_{ij}} \right)^2 \quad (14)$$

250 PMF was implemented on all datasets unconstrainedly through the Source Finder software (SoFi version 9.5,  
251 Canonaco et al. 2013) with 100 runs which are posteriorly sorted as in BAMF. The number of runs may seem  
252 compromising the PMF quality in comparison to the 4000-12000 samples per chain used in Bayesian models.  
253 However, this comparison is misleading, since the factorisation space is indeed better explored by PMF, with 100

254 different sampling seeds, while only 4 seeds (chains) were used in BAMF-like models as usual procedure in  
255 Bayesian modelling for the sake of computational resources.

256

### 257 **2.3 Pre- and post- processing for all models**

258 Before model running,  $\mathbf{X}$  and  $\sigma$  are normalised to use consistent scales of all priors and posteriors for Bayesian  
259 models. The normalisation is based on ensuring a mean of  $\mathbf{X} = 1$ .

$$260 \quad X^* = X / f_{norm} \quad , \quad \sigma^* = \sigma / f_{norm} \quad \text{where} \quad f_{norm} = \sum_{i,j} X_{ij} / (n \cdot m) \quad (15)$$

261 After the factorisation this normalisation is reverted converting the normalised matrices, hereinafter referred as  $\bar{G}$ ,  
262  $\bar{F}$ , to the properly-scaled  $\mathbf{G}$ ,  $\mathbf{F}$  matrices.

263

264 The factor ordering in the matrices is random in the model results, hence, the solution factors must be sorted.  
265 Here, as in Rusanen et al. (2024), we used the Hungarian algorithm (Kuhn, 1955) to sort the  $\bar{Z}_k$  components  
266 ( $\bar{Z}_k = \bar{G}_{ik} \cdot \bar{F}_{kj}$ ), i.e. each factor's normalised  $\mathbf{Z}$  submatrix). The metric to sort the components is the Manhattan  
267 distance (i.e. the sum of the absolute differences of two Cartesian coordinates). All factors in each chain of samples  
268 are then reordered upon the factor order of a small group of samples of that chain (the last 5, arbitrarily chosen)  
269 and, subsequently, one all-samples-averaged  $F_k$  and  $G_k$  are retrieved for each of the chains. Then, the order of  
270 factors of each of the chains is sorted again in the same way in relation to the truth  $\mathbf{F}$ , to have all sources equally  
271 sorted in all chains. Median and quantiles are computed over samples and chains to produce the final solutions  
272 and uncertainties. This sorting process is also used for the PMF solution despite not being its usual sorting  
273 approach for the sake of homogeneity in comparison to the Bayesian models.

274

275 The last step of the experimental process was to assess the model performance on the given dataset. The evaluation  
276 of the performance should be based on: i. reconstruction performance, or the difference between  $\mathbf{X}$  and  $\mathbf{Z}$ ; ii.  
277 similarity to truth, or environmental sensibility based on the apportionment of source tracers in case the truth is  
278 not available; iii. computational performance. The reconstruction performance was assessed by checking the cell-  
279 wise correlation between  $\mathbf{X}$  and  $\mathbf{Z}$  and checking the median and maximum of the absolute value of relative  
280 deviations of  $\mathbf{Z}$  and  $\mathbf{X}$  with respect to the measurement uncertainty matrix  $\sigma$  ( $|\mathbf{X}-\mathbf{Z}|/\sigma$ ). The similarity to truth,  
281 when available, is tackled by comparing the median ratio between modelled  $\mathbf{G}$  and truth ( $\mathbf{G}/\mathbf{G}_0$ ), the Pearson  
282 correlation for the  $\mathbf{G}$  matrix ( $\mathbf{G} \rho$ ), and the Spearman correlation for  $\mathbf{F}$  amongst models ( $\mathbf{F} \rho$ ). The Spearman  
283 correlation coefficient for the factor profiles was chosen due to the expected non-linearity of the comparison and  
284 likely presence of outliers. These comparisons, and especially when the ground truth is not available, need to be  
285 accompanied by visual inspection of the solution quality, looking for resemblance with known environmental  
286 sources. The models accounting for sparsity will be also compared upon the aforementioned Gini metric and,  
287 when truth is available, the Gini ratio with truth and the “zero-truth sum”. Computational performance assessment  
288 will be based on the metrics of convergence metrics of the Hamiltonian-Montecarlo Markov chain methods  
289 embedded in STAN software (e.g.  $\hat{R}$ ).

290

## 291 2.4 Datasets

292 The datasets created for model experimentation can be divided into synthetic and real-world datasets. Synthetic  
293 datasets are artificially created with the purpose of knowing the  $\mathbf{F}$ ,  $\mathbf{G}$ , to test model accuracy retrieving these  
294 matrices with respect to the *truth* and these have been widely used for source apportionment validation in the last  
295 decades (Park et al. 2002, Brinkman et al. 2006; Belis et al. 2015; Via et al. 2022; Rusanen et al. 2024). In order  
296 to challenge the models gradually, we created three synthetic datasets with increasing degrees of complexities  
297 (toy, offline, online ACSM synthetic datasets). Additionally, a real-world chemically sparse dataset was also used  
298 to test the results. Although the truth factorisation is unknown and the results cannot be directly verified, the  
299 model's factorisation can be assessed environmentally or based on indicators on the goodness of fit. The different  
300 datasets have different levels of sparsity, as can be seen in Table 2, that the models with the horseshoe prior should  
301 aim to replicate. The time resolution of modelled OA sources, used both in the chemically-sparse toy dataset and  
302 the chemically less sparse datasets, is 1 hour. The time resolution of offline datasets, used in the chemically sparse  
303 synthetic offline dataset and the chemically-sparse real-world offline dataset is 1 day.

### 304 2.4.1 Chemically-sparse toy dataset

305 A simplistic synthetic toy dataset was designed as a deliberately simplified test case to perform basic control and  
306 performance tests, rather than to reproduce any realistic atmospheric scenario. It was devised by creating three  
307 very simple and sparse profiles and using three time series (HOA, SOA<sub>bio</sub>, BBOA) from modelled source time  
308 series of the city of Zurich (Rusanen et al. 2024, time resolution of 1h) in order to test how sparsity priors act on  
309 very uneven species contribution. Although it is based on ACSM-like time series and therefore reflects some of  
310 the temporal properties of such measurements, the three included sources do not represent combinations that  
311 would be expected in a real-world environment since this toy dataset is intended solely for methodological testing  
312 purposes. In addition, the source profiles were intentionally designed to be highly simplified in order to facilitate  
313 an immediate visual assessment of the model fitting. For these reasons, the extracted components were not  
314 assigned environmental labels, but were instead referred to generically as Factor 1, Factor 2, and Factor 3.

315  
316 Then,  $\mathbf{F}$  and  $\mathbf{G}$  were multiplied to generate  $\mathbf{Z}$ , and some gaussian error with standard deviation  $\sigma$  was added to  
317 each component to generate a realistic  $\mathbf{X}$  matrix. The uncertainties matrix  $\sigma$  was designed as a sixth of the  $\mathbf{X}$  values  
318 plus Gaussian noise. With this arrangement, the models can be applied conventionally to the  $\mathbf{X}$ ,  $\sigma$  matrices and  
319 the modelled  $\mathbf{F}$  and  $\mathbf{G}$ , can be compared to the original truth  $\mathbf{F}_0$  and  $\mathbf{G}_0$ , which will be referred hereinafter as  $\mathbf{F}_0$  and  $\mathbf{G}_0$ ,  
320 displayed in Figure S2.

### 321 2.4.2 Chemically-sparse synthetic offline dataset

322 We created a synthetic offline filter dataset, mimicking the filter-based measurements input matrices, in order to  
323 test the accuracy of the models in these kinds of datasets. This dataset mimics the concentrations on the coarse  
324 fraction (PM<sub>10</sub> - PM<sub>2.5</sub>) as collected by a high-volume sampler on the Zurich-Kaserne site (Grange et al. 2021)  
325 including the following chemical species: OC, Al, Na, Mg, Cl, K, Ca, S, Fe, Cu, Zn, Mn, Sb, Ba, mannitol,  
326 arabitol. In the original real-world dataset, data obtained with two series of samples (PM<sub>10</sub> and PM<sub>2.5</sub>) were  
327 subtracted in order to focus on the coarse source apportionment, since the main emission sources of these elements  
328 and organic species stem from mechanical processes leading to major coarse models. It was created by crafting

329 first the **F** and **G**, then multiply them and creating **X** and  $\sigma$ . The **F** matrix was slightly modified from that proposed  
330 in Manousakas et al. (2025), making the chemical profiles slightly sparse by zeroing the non-relevant species in  
331 each of the factors (dust, traffic, salt, coarse biological). The **G** matrix was composed of the time series of:

- 332 - Dust: modelled PM<sub>10</sub> dust (Vasilakos et al. in prep.) converted to coarse with the Al<sub>PM10</sub> vs. PM<sub>10</sub> ratio  
333 from Grange et al. (2021).
- 334 - Traffic: modelled PM10 copper (Upadhyay et al. 2025) converted to coarse with the Cu<sub>PM10</sub> vs. PM<sub>10</sub>  
335 ratio from Grange et al. (2021).
- 336 - Salt: coarse Na+Cl (Grange et al. 2021) converted to PM concentrations and multiplied by an arbitrary  
337 number (3 in this case match the concentrations of the sea salt factor in the original dataset).
- 338 - Coarse biological: coarse Arabitol+Mannitol (Grange et al. 2021) converted to PM concentrations and  
339 multiplied by 3, similarly as for the salt factor.

340 This dataset will be called “offline synthetic dataset”. Another more simplistic dataset was prepared similarly but  
341 using Al and Cu for dust and traffic factors, respectively, in the same way as in the salt or coarse biological factors,  
342 i.e. omitting the use of modelled data. This dataset will be hereinafter named “Purely-measurement-based offline  
343 synthetic dataset” and its modelling results will be described in section 3.2. Once the **F** and **G** matrices were  
344 created, **X** was calculated by their multiplication and the addition of Gaussian noise with amplitude  $\sigma$ . The  
345 uncertainties matrix  $\sigma$  was generated as in Grange et al. (2021) multiplied by 2 to balance the signal-to-noise ratio  
346 to the datasets in Manousakas et al. (2025). The matrices **F**, **G** of this dataset are displayed in Figure S3.

347

### 348 **2.4.3 Chemically sparse real-world offline dataset**

349 A real-world dataset was employed to test the current models applicability in campaign measurements. This  
350 dataset was originally used for source apportionment in Manousakas et al. (2025) and Grange et al. (2021) and  
351 consists of PM<sub>10-2.5</sub> samples at five Swiss National Air Pollution Monitoring Network (NABEL): Basel, Bern,  
352 Magadino, Payerne, and Zurich. The measurements were taken in the June 2018 - July 2019 period every fourth  
353 day and using Digital high-volume samplers. During the sampling campaign PM<sub>10</sub> and PM<sub>2.5</sub> were collected and  
354 the respective concentrations were subtracted to generate the coarse (PM<sub>10-2.5</sub>) concentrations. These samples  
355 include: i. OC concentrations, measured through the thermal optical transmission (TOT) EN16909 method with  
356 the EUSAAR2 temperature protocol; ii. elemental concentrations (Al, Fe, Cu, Zn, Mn, Sb, Ba, Sr, Bi, Pb)  
357 measured by inductively coupled plasma atomic emission spectrometry (ICP-AES) and inductively coupled  
358 plasma mass spectroscopy (ICP-MS); iii. water soluble inorganic ion concentrations (Ca<sup>+</sup>, Cl<sup>+</sup>, Mg<sup>+</sup>, K<sup>+</sup>, Na<sup>+</sup>),  
359 determined by ion chromatography (IC); iv. Organic species (mannitol, arabitol) determined by a high-  
360 performance liquid chromatographic method followed by pulsed amperometric detection (HPLC-PAD). The  
361 uncertainties of these species were calculated as in Grange et al. (2021).

### 362 **2.4.4 Chemically less sparse synthetic online ACSM datasets**

363 With the aim of recreating more complex real-world datasets to test the models, we generated 6 datasets for four  
364 European cities: Krakow, Milan, Paris, and Zurich. The objective was to recreate OA matrices as given by a mass  
365 spectrometer instrument like Q-ACSM, for which there are plenty of real-world source apportionment studies in  
366 the literature. The **G** matrix was created from OA sources time series generated through the regional air quality

367 model CAMx (Comprehensive Air Quality Model with Extensions) as previously published by Jiang et al. (2019).  
 368 The five sources of these datasets were hydrocarbon-like OA (HOA), related to traffic emissions, biomass burning  
 369 OA (BBOA), biogenic SOA ( $SOA_{bio}$ ), biomass burning SOA ( $SOA_{bb}$ ), and traffic SOA ( $SOA_{tr}$ ). To ensure  
 370 seasonal representativity while keeping computational costs low, datasets included the first two weeks of every  
 371 second month of 2011 (January, March, ...). The relative concentrations of these datasets are shown in Figure S5.  
 372 This figure shows the highest seasonal OA variation for the city of Milan and the lowest for Zurich. In terms of  
 373 sources, the most seasonally stable sources, overall, are HOA and  $SOA_{tr}$  in contrast to the remarkable variability  
 374 of BBOA and  $SOA_{bio}$ . The profiles used to create the species matrix  $\mathbf{F}$  were those in Table S2 for primary sources  
 375 (HOA, BBOA). For secondary sources, the profiles from the European megacity dataset presented in Rusanen et  
 376 al. (2024) were used for the Zurich city, which were slightly perturbed for the other cities due to the limited  
 377 availability of these sources' profiles in the literature.

378

379 The  $\mathbf{X}$  matrix was obtained by multiplying the  $\mathbf{F}$  and  $\mathbf{G}$  submatrices and adding Gaussian noise. The procedure to  
 380 calculate the error matrix for such datasets is described in Via et al. (2022) and the dataset used to calculate the  
 381 error matrix is that from the Zurich site, which ranges from February 2011 until December 2011.

382

383 Lastly, a sensitivity analysis was carried out by slightly modifying the original  $\mathbf{F}$ ,  $\mathbf{G}$  matrices upon which the  $\mathbf{X}$ ,  
 384  $\sigma$  matrices were subsequently created. The first Zurich dataset (period 01/09/2011 - 14/09/2011) was used for this  
 385 purpose and we chose to perturbate one factor only (HOA). The  $\mathbf{F}$ ,  $\mathbf{G}$  submatrices were perturbed independently  
 386 upon the expression:

$$387 \quad G_{HOA}' = G_{HOA} \cdot N(1, \sigma') \quad F_{HOA}' = F_{HOA} \cdot N(1, \sigma') \quad (14)$$

388 where we used  $\sigma' = [0, 0.1, 0.2, 0.3, 0.4, 0.5]$  to create different degrees of perturbation. The profiles in  $\mathbf{F}$  were  
 389 normalised after that process. It must be noted that the perturbation is more relevant on  $\mathbf{F}$  than in  $\mathbf{G}$  since a given  
 390  $\sigma'$  in the aforementioned range is more comparable and impactful on the profile contributions, bounded to 1, than  
 391 on the unbounded time series timepoints. Consequently, within this framework, we obtained 6  $\mathbf{G}$ -perturbed and 6  
 392  $\mathbf{F}$ -perturbed input matrices. Both BAMF and BAMF+HS models were run with all these input matrices and their  
 393 subsequent HOA results were compared to the original truth in order to comprehend the sensitivity of the models  
 394 upon time series and profile perturbations.

### 395 **3. Results**

#### 396 **3.1 Chemically sparse synthetic toy dataset**

397 Here, we introduce the evaluated models relying on unrealistically simplified toy data with the purpose of  
 398 showcasing the performance of the horseshoe prior introduction to BAMF (Figure S2) and the alternative  
 399 factorisation methodologies, which are discussed in SI Section C.1.

400

401 In the first evaluation step, we assess the performance of the horseshoe prior under the assumption that the source  
 402 matrix  $\mathbf{G}$  is known, in order to isolate its effect on the estimation of  $\mathbf{F}$ . Figure 1 shows the distribution of each  $\mathbf{F}$   
 403 component for CMB with and without the horseshoe prior (CMB, CMB+HS, respectively, Table 1). The  
 404 distributions shown account for all the variability across samples of each  $\mathbf{F}$  component for both models, and the

405 truth is shown as a marker in the x-axis since it is a point value to be compared to the centers of the distributions.  
406 The presentation of the CMB and CMB+HS distributions aims to demonstrate the sparsity-inducing role of the  
407 horseshoe prior, which enforces shrinkage of the F component toward zero; this effect is more readily discernible  
408 when a strongly guided G matrix is used to isolate the evidence of sparsity. Figure 1 showcases the horseshoe  
409 prior power to generate sparsity in F components, shrinking more strongly the lowest signals to zero than CMB  
410 and, as a consequence, enlarging the most prominent signals. Table 3 shows how the Gini metric is consistently  
411 higher for CMB+HS with respect to CMB, supported by a higher Gini ratio and lower zero truth metric reflecting  
412 the sparsification of profiles and higher similarity to truth. The RMSE compared to the truth for the profiles  
413 improved with the horseshoe prior applied for all three factors (for CMB and CMB+HS, respectively: 1.2e-04,  
414 3.8e-05 for F1; 1.86e-04, 5e-05 for F2; 3.3e-05, 1e-05 for F3). Hence, the sparsity introduced in F through the  
415 regularised horseshoe prior successfully improved the profile description of the solution.

416  
417 In the next evaluation step, we test the various models assuming no prior knowledge. Figure 2 shows the results  
418 of PMF, BAMF, and BAMF+HS models on the toy dataset and Table 3 shows their factorisation performance  
419 and comparison to truth metrics. In terms of factorisation, median relative errors are better for BAMF+HS and  
420 BAMF than for PMF, but their maximum errors are higher and the Pearson coefficients slightly lower, all this  
421 entailing comparable factorisation performances. All models generally adapt well to the truth features, but they  
422 present non-negligible differences. PMF results better resemble the truth in terms of  $\mathbf{G} R^2$ , but it is the model  
423 whose  $G/G_0$  differs from 1 the most, accumulating the greatest error (2.64), followed by BAMF (2.10), while  
424 BAMF+HS exhibits the smallest deviation (0.81), indicating the highest overall accuracy. In terms of profiles, the  
425 BAMF+HS model is the closest to the truth both in terms of  $\rho$  and  $R^2$ , especially for the second and third factors  
426 for which the sparsity introduction results are advantageous with respect to BAMF results. Consistently, the Gini  
427 ratios of the inferred solutions relative to the truth are markedly closer to unity for BAMF+HS (range 0.40–0.93)  
428 than for PMF (0.45–0.64). The sparsity effects can also be seen in Figure S5, in which the horseshoe shrinkage is  
429 evident for the low m/zs allowing in turn the larger m/zs to retain more mass, hence resembling better the truth  
430 profiles. Taken together, these results indicate that BAMF+HS not only promotes sparsity, but does so in a  
431 chemically consistent manner, leading to a more accurate mass apportionment across factors, despite a slightly  
432 reduced time-series correlation for the third factor. However, the BAMF+HS could not shrink down the lowest  
433 signals in Factor 1, likely because their contribution estimated by the mass balance and the autocorrelation  
434 restrictions of this model made it unclear for the horseshoe to shrink them down completely. With this result, this  
435 toy dataset depicts the capacities and limitations of the horseshoe implementation on BAMF: it is capable to  
436 sparsify effectively only the signals which are close enough to zero as given by the restrictions of the BAMF  
437 model.

438 While other sparsity priors exist (e.g. Lasso and Spike-and-slab priors (Figure S6, Table 3, Table S3)), our tests  
439 show that the BAMF+HS model is most effective in shrinking unnecessary contributors to F. Hence this prior  
440 will be used onwards. This is evidently portrayed by the Gini ratio, for which neither Lasso nor Spike-Slab achieve  
441 the signal shrinkage that the BAMF+HS does. Also, neither BAMF+Lasso nor BAMF+Spike-and-slab managed  
442 to sparsify the first factor. Additionally, different autocorrelation formulations were implemented with and  
443 without the horseshoe prior, showing worse performance than BAMF or BAMF+HS, respectively, as discussed  
444 in section SI C.1. This supports using the BAMF autocorrelation prior instead of the alternative AR(1) prior, G

445 simplex formulation or lack of autocorrelation prior models, although these models are also tried on the other  
446 datasets to further highlight this.

### 447 **3.2 Chemically sparse synthetic offline dataset**

448 This synthetic offline dataset was used to assess the performance of different models on a proxy representation of  
449 atmospheric aerosol data, while maintaining the verifiability property inherent to synthetic datasets as described  
450 in Section 2.4.2. We performed source apportionment of the  $\mathbf{X}$  matrix through the aforementioned Bayesian  
451 models and PMF, obtaining 4 factors fingerprints and time series. The dataset used in this source apportionment  
452 is expected to be much more sparse than ACSM-like datasets, hence it could better expose the capabilities and  
453 added value of the sparsity prior.

454  
455 To avoid initialisation failure, BAMF was run by initialising  $\mathbf{F}$  as a normal distribution to ensure a more sturdy  
456 sampling. Model initialisation fails when no set of initial parameter values satisfying the model result in valid  
457 Bayesian solutions, and are usually solved by imposing more informative priors constraints on the model  
458 parameters. A t-test was run comparing the  $\mathbf{F}$ ,  $\mathbf{G}$  factors from this slightly modified model and BAMF to ensure  
459 their similarity. Its results passed the t-test for all factors except for one factor, although it presented a  $R^2=0.9990$   
460 correlation and only a 20% of quantitative difference with that BAMF factor. Hence, one can assume that the  
461 model provides an acceptable level of agreement with BAMF, capturing the essential structure of the factors with  
462 only very minor deviations.

463  
464 Figure 3 presents the (a) time series (b) auto-correlation (c) profiles of the source apportionment solution for PMF,  
465 BAMF, BAMF+HS, (d) additional comparison to truth metrics, and Figure 4 shows the histograms of the models  
466  $\mathbf{F}$  components estimation. The time series and autocorrelation show only slight differences between the models,  
467 the PMF being the most different to the truth in all factors except the salt one, as supported in Figure 3 (d).  
468 Amongst factors, the coarse biological source is the most poorly reconstructed. If accounting for the sum of all  
469 factors  $\mathbf{G} R^2$ s and  $\mathbf{G}/\mathbf{G}_0$ , in the last row of Figure 3(d), the most accurate model is the BAMF+HS, followed by  
470 PMF and then BAMF. In terms of profiles, the best overall model performance depends on the metric,  $\mathbf{F}$  Spearman  
471 correlation coefficient being highest for BAMF and  $R^2$  and cosine similarity correlation coefficients for  
472 BAMF+HS. This fact, accompanied by Gini being the highest for BAMF+HS and the closest to 1 Gini ratio,  
473 indicates that the extreme values of the profile (i.e. maximum and zeros species contributions) are closer to truth  
474 for BAMF+HS, whose extreme contributions would be less relevant in the Spearman correlation coefficient.  
475 Considering the Truth  $\mathbf{F}$  zeros sum metric, the horseshoe shrinkage is visibly sparsifying most of the low signals  
476 whilst BAMF and PMF present non-zero contributions for species whose contribution in this factor is null. Hence,  
477 the BAMF+HS model would effectively promote the profiles sparsity which it was intended for.

478  
479 However, the favourable results of BAMF+HS in comparison to the other models could be a dataset-dependent  
480 finding, related to the properties of the created synthetic dataset. The purely-measurement-based offline synthetic  
481 dataset, whose performance statistics are shown in Table S4, shows that PMF overperforms BAMF+HS,  
482 presenting slightly higher  $\mathbf{F}$  and  $\mathbf{G} R^2$  and better  $\mathbf{G}/\mathbf{G}_0$ . This could indicate that the optimal model selection might  
483 be dataset dependent. However, the source time series of this very simplistic dataset are fully correlated with some

484 species time series, since they are used to generate factor time series, which makes it a very redundant dataset. In  
485 this scenario, the source apportionment comparison might still be valid, but it is not the perfect showcase for RMs  
486 testing due to the excessive source correlation with species. We found it valuable to present different model  
487 performances on different datasets, which in atmospheric measurements, can suffer from artefacts complicating  
488 the behaviour of some models.

489

490 In the same way, the alternative autocorrelation priors models were also tried and will be thoroughly discussed in  
491 Section SI C.II. However, overall, the BAMF+HS model is the one providing the best source apportionment  
492 results for this offline dataset, taking advantage of the sparsity to upgrade both profiles and time series accuracy.

493

### 494 **3.3 Real-world offline dataset**

495 To test the models on real-world data and identify their limitations for more complex datasets, we tested the  
496 models in the real-world offline PM<sub>10</sub>-PM<sub>2.5</sub> dataset described in Section 2.4.3. Since the truth is not accessible,  
497 the model performance can only be assessed upon environmental, factorisation-related, and coputational criteria.  
498 For this dataset, BAMF and BAMF-AR1 models presented initialisation issues preventing them from properly  
499 launching the models. To avoid this issue and make the model more robust, we implemented a prior in **F** so that  
500 its components are drawn from Gaussian distributions centered at zero and with a standard deviation of 1 so that  
501 we restrict values to be bounded to 1. This modification was not needed for the other models, which did not present  
502 initialisation issues.

503

504 Source apportionment results for PMF, BAMF, and BAMF+HS are shown in Figure 5 and Table 4. Figure 6  
505 shows the **F** distributions for these models, as a detail of Figure S9 (a). Figure S6, S9 (a) display very similar  
506 results for PMF, BAMF, BAMF+HS both in terms of **F**, **G**, and reconstruction metrics, and only some differences  
507 can be perceived for PMF, while BAMF and BAMF+HS histograms are almost overlapping in Figure 6. However,  
508 the BAMF+HS profiles present a remarkable difference in terms of sparsity as seen in the **F** Gini metric, which is  
509 mostly the highest for BAMF+HS or equal, except for the biological factor for which PMF is slightly higher. For  
510 some species, the relative **F** components apportionment is more strongly suppressed by BAMF+HS than by  
511 BAMF or PMF, hence, their contribution on other profiles can be larger. This is clearly visible, for instance, for  
512 OC, Mg<sup>+</sup>, K<sup>+</sup>, S<sup>+</sup>, or mannitol, which are zeroed in the Salt factor and consequently are larger on the factors where  
513 these species are relevant. This is more evidently depicted in Figure S9 (a) and Figure 6, where the distribution of  
514 **F** components is shown. For the aforementioned species, the horseshoe effect can be seen in the distribution,  
515 whilst BAMF and PMF are further from zero. This result thus highlights the potential benefits of sparsity  
516 introduction in matrix factorisation.

517

518 The application of other autocorrelation priors was not advantageous with respect to the regular BAMF  
519 autocorrelation and even worsened the shrinkage power of the horseshoe prior as discussed in SI C.III.

### 520 3.4 Chemically less sparse synthetic online ACSM datasets

521 The next step was to test these models on more realistic synthetic datasets. For that purpose, 6 datasets for 4  
522 European cities (a total of 24 datasets) were designed with 5 factors in each of them (section 2.4). We applied the  
523 8 models under discussion (PMF, BMF, BMF+HS, BAMF, BAMF+HS, BAMF-AR1, BAMF-GS) to the 24  
524 synthetic datasets and computed the summary statistics (the median of the ratios of  $\mathbf{G}$  over the truth  $\mathbf{G}$ ,  $\mathbf{G}/\mathbf{G}_0$ , the  
525 Pearson correlation of  $\mathbf{G}$  with truth,  $\mathbf{G}_r$ , and the Spearman correlation of  $\mathbf{F}$  with truth,  $\mathbf{F}_\rho$ ). All metrics over cities,  
526 datasets and sources are presented in Table S5, and an example for one site (Zurich) and one dataset (dataset 0,  
527 from 01/01/2019 to 14/01/2019) is shown in Figure S11 as an example of the results obtained by the three models  
528 in 1 out of the 24 datasets.

529  
530 Figure 7 shows the model summary statistics over the 6 generated datasets for the four cities and Figure S12 shows  
531 the factor-dependent statistics. In this case, the (not-squared) Pearson correlation coefficient was used to compare  
532 the results of the ACSM-like datasets more easily to those presented in Rusanen et al. (2024), which used this  
533 metric. Figure 7 shows a good agreement between models and the truth, with most solutions with correlations  
534 with truth for  $\mathbf{F}$  and  $\mathbf{G}$  above 0.7, similarly to Rusanen et al. (2024). However, there are clear differences amongst  
535 models and cities. PMF is performing worse in comparison to the Bayesian models, including BMF, the Bayesian  
536 analog to PMF in all datasets except for Milan. As shown in Table S5, PMF presents the highest  $|\mathbf{Z}-\mathbf{X}|/\sigma$ , the  
537 highest overestimations of  $\mathbf{G}$ , and correlations of  $\mathbf{G}$  and  $\mathbf{F}$  are the lowest in comparison to other models except for  
538 the Milan dataset. In terms of  $\mathbf{G}/\mathbf{G}_0$ , the model providing the best results are BAMF, BAMF-AR1, BAMF-GS,  
539 followed by their horseshoe versions. The BAMF+HS, presents slightly lower  $\mathbf{F}_\rho$ ,  $\mathbf{F}_R^2$ , and the sparsity Gini  
540 metric ratio is not close to one, entailing the horseshoe prior did not successfully implement sparsity and the  $\mathbf{F}$   
541 accuracy did not improve. In terms of correlations with  $\mathbf{F}$  and  $\mathbf{G}$ , the models including the horseshoe prior present  
542 higher dispersion within a city with respect to the models without sparsity terms. Considering all the parameters,  
543 the models with the best overall performance are BAMF, BAMF-GS, and BAMF+HS.

544  
545 Figure S13 shows the autocorrelation for lags 0-168 h (half of the monthly measurement period) for all the sources  
546 and sites, displaying the cyclicity of the selected sources. In all cases, the short-term lags present very high  
547 autocorrelation, entailing that the similarity on adjacent timestamps is very high and decays over longer periods.  
548 Typically, and as presented on the figure, the autocorrelation of primary sources, with more marked daily cycles,  
549 decays faster than secondary sources, which evolve more steadily due to their slower reaction to emissions. Whilst  
550 HOA and BBOA present a very steady intradaily structure, with one or two maxima per day, the biogenic SOA  
551 presents one peak per day and the other two secondary sources may or may not present marked daily cycles. This  
552 different intra- and inter-daily structure amongst sources certainly challenges the models to resolve the source-  
553 dependent characteristic.

554  
555 Figure 8 shows the autocorrelation from truth and the model outputs correlate (Pearson coefficient of  
556 determination) for each model and source in the 4 cities. Each dot represents one of the 6 datasets for each site,  
557 and colors represent the different sources. The results show that all models present very high Pearson coefficient  
558 ranges for  $\mathbf{G}$  autocorrelations in comparison to truth except for PMF, which struggles with this dataset aspect due  
559 to the lack of accounting of self-correlation. In general terms, the best captured correlation by all models is that

560 of  $SOA_{Bio}$ , with the most regular cyclical patterns. The  $SOA_{BB}$  and  $SOA_{Tr}$  autocorrelations seem to challenge the  
561 models further due to more irregular patterns, and for some datasets, their autocorrelation is poorly modeled. POA  
562 sources are generally accurately modelled, with HOA patterns slightly better captured than those from BBOA.  
563 Regarding models, the ones with better performance are BAMF-GS, BAMF, and BAMF+HS, with only slight  
564 differences between the last two. This observation suggests that the horseshoe prior addition does not significantly  
565 reduce the autocorrelation power of the BAMF.

566

567 Regarding sparsity, Figure S14 depicts the lack of sparsity both for input and modelled data. This figure shows  
568 the truth's 5 lowest  $m/z$  components as well as BAMF, BAMF+HS outcomes. The reference (truth) profiles do  
569 not present zeros but very small signals, as do many ACSM-like profiles in the AMS spectral database (Ulbrich  
570 et al. 2009). Both BAMF, BAMF+HS reflect this lack of sparsity, however, it could be expected that BAMF+HS  
571 would decrease the contributions of the lowest components. However, the sparsity introduction was not achieved  
572 as seen before in the lack of improvement of the Gini ratios. This lack of sparsity despite the enforcement through  
573 the horseshoe prior can be explained by the complexity of the data, which due to chain divergence, hinders the  
574 models performance. Figure S15 shows the model  $\hat{R}$ , a typical Bayesian metric to evaluate the precision of  
575 Hamiltonian chains, computing the ratio between inter- and intra-chain variabilities. In any case results are very  
576 close to the ideal value, 1, so the validity of all models' solutions is assured. However, this plot reflects the  
577 deprecation of the solution with models when the horseshoe prior is applied. The horseshoe prior adds more  
578 complexity to the  $\mathbf{F}$  with three more parameters compared to non-sparsity models which could be the cause of the  
579 increased model instability across chains.

580

581 Finally, a sensitivity analysis was run for the first Zurich dataset perturbing independently the original  $\mathbf{F}$ ,  $\mathbf{G}$   
582 matrices to different degrees, monitoring the correlation of the modelled  $\mathbf{F}$ ,  $\mathbf{G}$  matrices to the original truth (Figure  
583 9). Subfigures (a) and (b) show how both in the case of the original  $\mathbf{F}$  and  $\mathbf{G}$  perturbations, the  $\mathbf{F}$  accuracy drops  
584 immediately and analogously for both models, with a more sudden decay for  $\mathbf{G}$  perturbations. Contrarily, the  
585 affectations in  $\mathbf{G}$  (subplots (c) and (d)) are different for both models, with a steady decay for BAMF with  $\mathbf{G}$   
586 perturbations and a non-clear trend for  $\mathbf{F}$  perturbations, whilst BAMF+HS correlation rests insensitive to  $\mathbf{F}$ ,  $\mathbf{G}$   
587 perturbations with an increasing/decreasing erratic behaviour. This result shows the reduced precision in  $\mathbf{G}$  of  
588 BAMF+HS in comparison to BAMF due to the chain divergence issue, which, in any case, does not severely  
589 compromise its accuracy. This finding also explains the bigger variations for BAMF+HS with respect to BAMF  
590 in all the metrics shown in Figure 8. Additionally, it showcases the general strong sensitivity of  $\mathbf{F}$  determination  
591 opposite to the general robustness of  $\mathbf{G}$  upon general  $\mathbf{X}$  matrix perturbation.

### 592 3. Discussion

593 This study aims to explore further BAMF capabilities and the benefits introduced through additional priors and/or  
594 modifications of the current model structure as given by Rusanen et al. (2024). The introduction of sparsity in  
595 source apportionment models was of particular interest to provide more distinct and concise source profiles which  
596 can, in turn, improve the time series accuracy. However, in real-world applications, it may also remove small but

597 relevant signals along with noise. Therefore, comparison with BAMF results is recommended, leaving it to the  
598 user to decide whether the method’s use is appropriate for their case.

599

600 Firstly, the use of the simplistic toy dataset highlighted the added value of the sparsity introduction through the  
601 horseshoe prior in the totally constrained experiment. In this controlled setting, the ground truth structure is well  
602 defined, allowing the effect of sparsity to be clearly isolated and the method performance validated. However, for  
603 an unconstrained experiment, sparsity was proven remarkably advantageous, but subject to the underlying matrix  
604 factorisation results. That is, the horseshoe prior in BAMF+HS effectively suppresses weak signals of  $\mathbf{F}$   
605 contributions as determined by BAMF, yet it fails to guide the model toward a more accurate or sparser solution  
606 when the initial BAMF estimate is suboptimal. Other sparsity priors, like Lasso and Spike-and-slab, were tried  
607 out but did not improve the regularised horseshoe performance.

608

609 The introduction of the regularised horseshoe prior in BAMF improved apportionment of offline synthetic and  
610 real-world datasets with respect to BAMF, promoting sparser profiles. The synthetic dataset comparison to truth  
611 was maximal for BAMF+HS, with sparser profiles and consequently better  $\mathbf{G}$  accuracy. Its application also proved  
612 advantageous for the real-world dataset, despite not being able to be compared to the truth. In this case,  
613 improvements are assessed through increased profile distinctness and internal consistency rather than absolute  
614 accuracy. The results show a sparsity effect which provides more distinct profiles in comparison to PMF and  
615 BAMF. This result encourages the usage of the horseshoe prior for sparsity introduction in datasets whose  
616 solutions are expected to be strongly sparse, such as elemental datasets.

617

618 Subsequently, in the more complex and realistic European datasets, the sparsity introduction could not be  
619 effectively enforced. Although solution quality was not substantially compromised, the profiles remained non-  
620 sparse after applying the prior. This is likely due to model instability arising from the higher complexity of these  
621 datasets, which is further aggravated by the addition of the horseshoe prior, as it requires sampling a larger number  
622 of parameters. Moreover, the inherent nature of ACSM datasets—characterized by highly correlated species—  
623 might also contribute to this limitation, since the model struggles to disentangle overlapping sources when  
624 variables are strongly interdependent. The higher chain divergence found for the *horseshoed* models causes a drop  
625 in solution precision due to different landings on the solution space depending on the chain. This issue could be  
626 reduced by selecting chains a-posteriori upon user-defined criterion as is practiced in PMF. This is further  
627 confirmed by the insensitivity to  $\mathbf{G}$  or  $\mathbf{F}$  perturbations that are visible for BAMF+HS but not for BAMF.  
628 Nonetheless, given that ACSM-like factor profiles exhibit low sparsity in the literature, the use of sparsity priors  
629 in these datasets is less justified. Also, because usually ACSM profiles obtained in chamber or ambient  
630 experiments are not usually sparse, as seen in Ulbrich et al. (2009), the BAMF+HS is not as pertinent in these  
631 kinds of datasets as for filter-based datasets.

632

633 The sparsity conceptual framework could also be brought into PMF through the pulling equations, which can  
634 shrink down manually the expectedly low signals in a factor. However, this methodology requires that the user  
635 indicates the species that are intended to be zeroed, which introduces user-subjectivity to the problem. The  
636 BAMF+HS method, contrarily, acts globally, shrinking those species with lowest signals in favour of the matrix

637 factorisation, hence no user intervention is needed. This makes the approach more objective but also less targeted,  
638 returning the factorization optimisation agency to the model. However, if the purpose were to enforce a shrinkage  
639 of a certain species as in the PMF case, this feature could also be implemented through the horseshoe method with  
640 minimal code modification.

641

642 The results of the other models tested (BAMF-AR1, BAMF-GS) did not show a significant improvement with  
643 respect to BAMF. The BAMF-AR1 contains another autocorrelation to parametrisation (STAN Team, 2025)  
644 which should allow for trend consideration, although this matter was not tackled in the current work and remains  
645 to be validated in future studies. The BAMF-GS seemed to capture slightly better the  $\mathbf{G}$  variability in comparison  
646 to BAMF in the online datasets, but led to worse correlation to truth in the offline synthetic dataset. Nonetheless,  
647 it does not support enforcing sparsity in  $\mathbf{F}$ , thereby reducing its effectiveness for profile adjustments.

#### 648 4. Conclusions

649 This study presents a sparsity introduction technique for the Bayesian Autocorrelated Matrix Factorisation model  
650 (BAMF) which intends to condense source apportionment profiles removing noisy signals. The regularised  
651 horseshoe prior is introduced in BAMF (BAMF+HS) in order to narrow down the lowest signals in factor profiles  
652 while keeping the most significant ones regularised. The BAMF+HS model is built in STAN, an open-source  
653 framework for statistical modelling with Hamiltonian-Montecarlo Markov Chain sampling. In order to test the  
654 capabilities of the developed model, we generated three kinds of synthetic datasets to compare the model  
655 factorisation outputs to the truth factors, namely Toy, offline, and online synthetic datasets, each representing a  
656 progressively increasing level of complexity. Likewise, to confirm its usability to real-world data, BAMF+HS  
657 was also applied to a multi-site filter dataset. Given the opportunity to explore source apportionment with different  
658 types of datasets, we also tested other receptor models such as Positive Matrix Factorisation (PMF) and other  
659 BAMF-like Bayesian models. In the Bayesian framework, we tested a different formulation of the autocorrelation  
660 term (BAMF-AR1) and a permutation on the factorisation matrix logic (BAMF-GS).

661 The main result highlights can be summarised as:

- 662 - BAMF+HS has been shown to be advantageous to introduce sparsity in factor profiles for offline datasets  
663 and to not deprecate the solution for the more complex datasets mimicking Aerosol Chemical Speciation  
664 Monitor (ACSM) data. Other sparsifying priors tried out were not as effective in low-signal shrinkage.
- 665 - The BAMF+HS performance towards truth profile reconstruction was higher than for BAMF and PMF  
666 in the toy and offline synthetic datasets. Improving  $\mathbf{F}$  typically led to a more accurate determination of  
667  $\mathbf{G}$ , highlighting the strong interdependence between the two factorisation matrices.
- 668 - The real-world dataset also shows a better description of sources through BAMF+HS in terms of matrix  
669 factorisation metrics and profile sparsification achievement.
- 670 - As shown in the toy dataset, the introduction of sparsity did not solve factorisation issues inherent to the  
671 underlying factorisation model.
- 672 - The BAMF+HS model does not create sparsity in ACSM-like datasets, which are originally, indeed, non-  
673 sparse. BAMF+HS is more unstable than BAMF for these more complex datasets as a result the higher  
674 chain divergence during Hamiltonian-Montecarlo Markov Chain sampling as suggested by the  $\hat{R}$  metric.

675            However, the effects of the horseshoe prior do not affect the overall performance of BAMF or its  
676            autocorrelation accuracy.

677            -    The alternative formulations for BAMF, BAMF-AR1 and BAMF-GS, did not show a significant  
678            improvement with respect to BAMF.

679            With all that, profile sparsity has been shown to substantially enhance the accuracy of source apportionment  
680            analyses, improving the separation of the chemical composition of sources. The BAMF+HS model succeeds in  
681            incorporating this property in profile fingerprints, especially in filter-based datasets. Using BAMF+HS in such  
682            datasets, the solutions reflect the sparsity of filter-based chemical profiles, hence, this newly introduced method  
683            is encouraged when source fingerprints are expected to be substantially sparse. However, for ACSM-like datasets,  
684            the sparsity is not fully achieved due to converge issues, although the quality of the solution is not substantially  
685            deprecated with respect to BAMF. With the aim of improving further source apportionment techniques, future  
686            research should be directed to enhance the robustness and generalisability of the BAMF+HS model across diverse  
687            data types. Moreover, continued exploration of the underlying properties of solution spaces (such as profiles  
688            sparsity, time series autocorrelation) may provide valuable insights into disentangling complex source  
689            contributions through receptor modelling. In this regard, the Bayesian source apportionment framework offers a  
690            particularly suitable foundation, allowing for the integration of prior knowledge and uncertainty quantification in  
691            the inference process.

## 692    **Code and data availability**

693    The models and datasets can be found at <https://github.com/martavia0/BAMF-horseshoe.git>

## 694    **Author contribution**

695    MV: Conceptualisation, data curation, formal analysis, funding acquisition, investigation, methodology, project  
696    administration, resources, software, validation, visualisation, writing (original draft preparation). YH: Formal  
697    analysis, investigation, software; JD: investigation, resources, software, validation. MM: Data curation. AR: Data  
698    curation, formal analysis, methodology, investigation, resources, software. JJ: Data curation. SKG: Data curation.  
699    J-LJ: Data curation; VNTD: Data curation. GU: Data curation. GM: conceptualisation, funding acquisition,  
700    investigation, supervision, validation. KRD: Conceptualisation, data curation, formal analysis, funding  
701    acquisition, investigation, methodology, supervision, validation. All co-authors participated in the revision and  
702    edition of the manuscript.

703

## 704    **Competing interests**

705    The authors declare that they have no conflict of interest.

706

## 707    **Disclaimer**

708

709    Co - funded by the European Union. Views and opinions expressed are however those of the author(s) only and  
710    do not necessarily reflect those of the European Union or European Research Exacutive Agency. Neither the  
711    European Union nor the granting authority can be held responsible for them.

## 712 **Acknowledgements**

713 This publication is co- funded by/ has received funding from/ the European Union’s Horizon Europe research and  
714 innovation program under the Marie Skłodowska-Curie COFUND Postdoctoral Programme grant agreement  
715 No.101081355- SMASH and by/from /the Republic of Slovenia and the European Union from the European  
716 Regional Development Fund. Work was partly supported by ARIS program P1-0385. All the chemical  
717 measurements on the PM10 and PM2.5 Swiss samples used in this study were performed on the Air O Sol  
718 analytical plateau at IGE (France). K.R.D. acknowledges support by the SNSF Ambizione grant PZPGP2\_201992.  
719 The authors thank Jimeng Wu and Imad El Haddad for their input related to autocorrelation.  
720

## 721 **References**

- 722 Andersen, M. R., Winther, O., & Hansen, L. K. (2014). Bayesian inference for structured spike and slab  
723 priors. *Advances in Neural Information Processing Systems*, 27.
- 724 Belis, C. A., Karagulian, F., Larsen, B. R., & Hopke, P. K. (2013). Critical review and meta-analysis of ambient  
725 particulate matter source apportionment using receptor models in Europe. *Atmospheric Environment*, 69, 94-108.
- 726 Belis, C. A., Larsen, B. R., Amato, F., El Haddad, I., Favez, O., Harrison, R. M., ... & Viana, M. (2014). European  
727 guide on air pollution source apportionment with receptor models. JRC reference reports EUR26080 EN.
- 728 Belis, C., Pernigotti, D., Karagulian, F., Pirovano, G., Larsen, B., Gerboles, M., and Hopke, P.: A new  
729 methodology to assess the performance and uncertainty of source apportionment models in intercomparison  
730 exercises, *Atmospheric Environment*, 119, 35–44, 2015.
- 731 Brinkman, G., Vance, G., Hannigan, M. P., and Milford, J. B.: Use of synthetic data to evaluate positive matrix  
732 factorization as a source apportionment tool for PM2. 5 exposure data, *Environmental science & technology*, 40,  
733 1892–1901, 2006.
- 734 Carpenter, B., Gelman, A., Hoffman, M. D., Lee, D., Goodrich, B., Betancourt, M., ... & Riddell, A. (2017). Stan:  
735 A probabilistic programming language. *Journal of statistical software*, 76, 1-32.
- 736 Crippa, M., DeCarlo, P. F., Slowik, J. G., Mohr, C., Heringa, M. F., Chirico, R., ... & Baltensperger, U. (2013).  
737 Wintertime aerosol chemical composition and source apportionment of the organic fraction in the metropolitan  
738 area of Paris. *Atmospheric Chemistry and Physics*, 13(2), 961-981.
- 739 Dai, T., Dai, Q., Yin, J., Chen, J., Liu, B., Bi, X., ... & Feng, Y. (2024). Spatial source apportionment of airborne  
740 coarse particulate matter using PMF-Bayesian receptor model. *Science of The Total Environment*, 917, 170235.
- 741 Daellenbach, K. R., Uzu, G., Jiang, J., Cassagnes, L. E., Leni, Z., Vlachou, A., ... & Prévôt, A. S. (2020). Sources  
742 of particulate-matter air pollution and its oxidative potential in Europe. *Nature*, 587(7834), 414-419.
- 743 Daellenbach, K. R., Manousakas, M., Jiang, J., Cui, T., Chen, Y., El Haddad, I., ... & Prévôt, A. S. H. (2023).  
744 Organic aerosol sources in the Milan metropolitan area–Receptor modelling based on field observations and air  
745 quality modelling. *Atmospheric Environment*, 307, 119799.
- 746 Dinh, V. N. T., Uzu, G., Dominutti, P., Sauvage, S., Elazzouzi, R., Darfeuil, S., Voiron, C., Samaké, A., Zhang,  
747 S., Socquet, S., Favez, O., and Jaffrezo, J.-L.: Toolbox for accurate estimation and validation of PMF solutions in  
748 PM source apportionment, *EGUsphere* [preprint], <https://doi.org/10.5194/egusphere-2025-1968>, 2025.

749 Elser, M., Huang, R. J., Wolf, R., Slowik, J. G., Wang, Q., Canonaco, F., ... & Prévôt, A. S. (2016). New insights  
750 into PM 2.5 chemical composition and sources in two major cities in China during extreme haze events using  
751 aerosol mass spectrometry. *Atmospheric Chemistry and Physics*, 16(5), 3207-3225.

752 Gelman, A., & Rubin, D. B. (1992). Inference from Iterative Simulation Using Multiple Sequences. *Statistical*  
753 *Science*, 7(4), 457–472. <https://doi.org/10.1214/ss/1177011136>

754 Gelman, A., Carlin, J. B., Stern, H. S., Dunson, D. B., Vehtari, A., and Rubin, D. B.: *Bayesian data analysis*, 3rd  
755 edn., CRC Press, ISBN 9781439898208, 2014.

756 Gini, Corrado (1936). "On the Measure of Concentration with Special Reference to Income and Statistics",  
757 Colorado College Publication, General Series No. 208, 73–79

758 Govan, E., Jackson, A. L., Inger, R., Bearhop, S., & Parnell, A. C. (2023). *simmr*: A package for fitting stable  
759 isotope mixing models in R. arXiv preprint arXiv:2306.07817.

760 Grange, S. K., Fischer, A., Zellweger, C., Alastuey, A., Querol, X., Jaffrezo, J. L., ... & Hueglin, C. (2021).  
761 Switzerland's PM10 and PM2.5 environmental increments show the importance of non-exhaust emissions.  
762 *Atmospheric environment: X*, 12, 100145.

763 Hoffman, M. D. and Gelman, A.: The No-U-Turn sampler: adaptively setting path lengths in Hamiltonian Monte  
764 Carlo, *J. Mach. Learn. Res.*, 15, 1593–1623, 2014.

765 Jiang, J., Aksoyoglu, S., El-Haddad, I., Ciarelli, G., Denier van der Gon, H. A., Canonaco, F., ... & Prévôt, A. S.  
766 (2019). Sources of organic aerosols in Europe: A modelling study using CAMx with modified volatility basis set  
767 scheme. *Atmospheric Chemistry and Physics Discussions*, 2019, 1-35.

768 Keuken, M. P., Moerman, M., Voogt, M., Blom, M., Weijers, E. P., Röckmann, T., & Dusek, U. (2013). Source  
769 contributions to PM2.5 and PM10 at an urban background and a street location. *Atmospheric Environment*, 71,  
770 26-35.

771 Kuhn, H. W. (1955). The Hungarian method for the assignment problem. *Naval research logistics quarterly*, 2(1-  
772 2), 83-97.

773 Lingwall, J. W., & Christensen, W. F. (2007). Pollution source apportionment using a priori information and  
774 positive matrix factorization. *Chemometrics and Intelligent Laboratory Systems*, 87(2), 281-294.

775 Liu, D. C. and Nocedal, J.: On the Limited Memory BFGS Method for Large Scale Optimization, *Math. Program.*,  
776 45, 503–528, <https://doi.org/10.1007/BF01589116>, 1989.

777 Manousakas, M. I., Rausch, J., Jaramillo Vogel, D., Schneider-Beltran, K., Alastuey, A., Jaffrezo, J. L., ... &  
778 Dällenbach, K. R. Comparison of PM Source Profiles Identified by Different Techniques and the Potential of  
779 Utilizing Single-Particle Analysis Data in Source Apportionment. Available at SSRN 5323830.

780 Metropolis, N., Rosenbluth, A. W., Rosenbluth, M. N., Teller, A. H., & Teller, E. (1953). Equation of state  
781 calculations by fast computing machines. *The Journal of Chemical Physics*, 21(6), 1087–1092.  
782 <https://doi.org/10.1063/1.1699114>

783 Oh, M. S., & Park, C. K. (2022). Regional source apportionment of PM2.5 in Seoul using Bayesian multivariate  
784 receptor model. *Journal of Applied Statistics*, 49(3), 738-751.

785 Paatero, P., & Tapper, U. (1994). Positive matrix factorization: A non-negative factor model with optimal  
786 utilization of error estimates of data values. *Environmetrics*, 5(2), 111-126.

787 Paatero, P. (1999). The multilinear engine—a table-driven, least squares program for solving multilinear  
788 problems, including the n-way parallel factor analysis model. *Journal of Computational and Graphical Statistics*,  
789 8(4), 854-888.

790 Park, E. S., Guttorp, P., & Henry, R. C. (2001). Multivariate receptor modeling for temporally correlated data by  
791 using MCMC. *Journal of the American Statistical Association*, 96(456), 1171-1183.

792 Park, E. S., Spiegelman, C. H., & Henry, R. C. (2002). Bilinear estimation of pollution source profiles and amounts  
793 by using multivariate receptor models. *Environmetrics*, 13(7), 775-798.

794 Park, E. S., Lee, E. K., & Oh, M. S. (2021). Bayesian multivariate receptor modeling software: BNFA and  
795 bayesMRM. *Chemometrics and Intelligent Laboratory Systems*, 211, 104280.

796 Piironen, J. and Vehtari, A.: Sparsity information and regularization in the horseshoe and other shrinkage priors,  
797 *Electronic Journal of Statistics*, 11, 5018–5051, <https://doi.org/10.1214/17-EJS1337SI>, 2017.

798 Rasmussen, M. A., & Bro, R. (2012). A tutorial on the Lasso approach to sparse modeling. *Chemometrics and*  
799 *Intelligent Laboratory Systems*, 119, 21-31.

800 Pope III, C. A., & Dockery, D. W. (1999). Epidemiology of particle effects. In *Air pollution and health* (pp. 673-  
801 705). Academic Press.

802 Rusanen, A., Bjorklund, A., Manousakas, M. I., Jiang, J., Kulmala, M. T., Puolamaki, K., and Daellenbach, K.  
803 R.: A novel probabilistic source apportionment approach: Bayesian auto-correlated matrix factorization,  
804 *Atmospheric Measurement Techniques*, 17, 1251–1277, <https://doi.org/10.5194/amt-17-1251-2024>, 2024.

805 Sage, A. M. (2007). Evolving mass spectra of the oxidized component of organic aerosol mass spectrometer  
806 analysis of aged diesel emissions. *Atmos. Chem. Phys. Discuss.*, 7, 10065-10096.

807 STAN Development Team. (2025). *Stan user's guide* (Version 2.36). <https://mc-stan.org/docs/stan-users-guide/>.  
808 Accessed July 2025.

809 Tobler, A. K., Skiba, A., Canonaco, F., Močnik, G., Rai, P., Chen, G., ... & Prevot, A. S. (2021). Characterization  
810 of non-refractory (NR) PM 1 and source apportionment of organic aerosol in Kraków, Poland. *Atmospheric*  
811 *chemistry and physics*, 21(19), 14893-14906.

812 Tibshirani, R., & Wasserman, L. (2015). Sparsity and the lasso. *Statistical machine learning*, 1-15.

813 Ulbrich, I. M., Handschy, A., Lechner, M., and Jimenez, J. L.: AMS Spectral Database,  
814 <http://cires.colorado.edu/jimenez-group/AMSsd/>, accessed: 2025-05-19, n.d.

815 Ulbrich, I. M., Canagaratna, M. R., Zhang, Q., Worsnop, D. R., & Jimenez, J. L. (2009). Interpretation of organic  
816 components from Positive Matrix Factorization of aerosol mass spectrometric data. *Atmospheric Chemistry and*  
817 *Physics*, 9(9), 2891-2918.

818 Upadhyay, A., Jiang, J., Cheng, Y., Vasilakos, P., Chen, Y., Banos, D. T., ... & El-Haddad, I. (2025). High-  
819 resolution modelling of particulate matter chemical composition over Europe: brake wear pollution. *Environment*  
820 *International*, 109615.

821 Via, M., Minguillón, M. C., Reche, C., Querol, X., & Alastuey, A. (2021). Increase in secondary organic aerosol  
822 in an urban environment. *Atmospheric chemistry and physics*, 21(10), 8323-8339.

823 Via, M., Chen, G., Canonaco, F., Daellenbach, K. R., Chazneau, B., Chebaicheb, H., Jiang, J., Keernik, H., Lin,  
824 C., Marchand, N., et al.: Rolling vs. seasonal PMF: real-world multi-site and synthetic dataset comparison,  
825 *Atmospheric measurement techniques*, 15, 5479–5495, 2022.

826 Viana, M., Kuhlbusch, T. A., Querol, X., Alastuey, A., Harrison, R. M., Hopke, P. K., ... & Hitzenberger, R.  
827 (2008). Source apportionment of particulate matter in Europe: a review of methods and results. *Journal of aerosol*  
828 *science*, 39(10), 827-849.

829 Yang, Y., Ruan, Z., Wang, X., Yang, Y., Mason, T. G., Lin, H., & Tian, L. (2019). Short-term and long-term  
830 exposures to fine particulate matter constituents and health: A systematic review and meta-  
831 analysis. *Environmental pollution*, 247, 874-882.

832 Zhang, Y., Albinet, A., Petit, J. E., Jacob, V., Chevrier, F., Gille, G., ... & Favez, O. (2020). Substantial brown  
833 carbon emissions from wintertime residential wood burning over France. *Science of the Total Environment*, 743,  
834 140752.

835 Zhang, Y., Ma, X., Tang, A., Fang, Y., Misselbrook, T., & Liu, X. (2023). Source Apportionment of Atmospheric  
836 Ammonia at 16 Sites in China Using a Bayesian Isotope Mixing Model Based on  $\delta^{15}\text{N-NH}_x$   
837 Signatures. *Environmental Science & Technology*, 57(16), 6599-6608.

838 Zheng, Y., Xue, T., Zhao, H., & Lei, Y. (2022). Increasing life expectancy in China by achieving its 2025 air  
839 quality target. *Environmental science and ecotechnology*, 12, 100203.

840 **Figures**

841 **Table 1. Models used in the current study and their priors on the G, F matrices.**

842

Model	G priors	F priors
BMF	None	None
BMF+HS	None	Regularised horseshoe
BAMF	Rusanen et al. (2024)	None
BAMF+HS	Rusanen et al. (2024)	Regularised horseshoe
BAMF-AR1	AR(1)	None
BAMF-AR1+HS	AR(1)	Regularised horseshoe
BAMF-GS	Rusanen et al. (2024)	None
PMF	None	None
CMB	Fixed a-priori.	None
CMB+HS	Fixed a-priori.	Regularised horseshoe

843

844 **Table 2. Profile sparsity metrics for the truth of synthetic datasets.**

845

Dataset	Factor	F Gini	% zeros
Chemically-sparse synthetic toy dataset	Factor 1	0.67	75.0
	Factor 2	0.67	75.0

	Factor 3		0.5	25.0
<b>Chemically-sparse synthetic offline dataset</b>	Dust		0.74	37.5
	Traffic		0.86	12.5
	Salt		0.78	37.5
	Coarse biological		0.88	25.0
<b>Less chemically-sparse synthetic online ACSM datasets</b>	HOA	Krakow	0.74	5.0
		Milan	0.67	0.0
		Paris	0.68	0.0
		Zurich	0.68	0.0
	BBOA	Krakow	0.47	1.2
		Milan	0.72	0.0
		Paris	0.74	0.0
		Zurich	0.58	0.0
	SOA <sub>bio</sub>	Krakow	0.52	0.0
		Milan	0.50	0.0
		Paris	0.50	0.0
		Zurich	0.67	0.0
	SOA <sub>BB</sub>	Krakow	0.55	0.0
		Milan	0.53	0.0
		Paris	0.53	0.0
		Zurich	0.73	0.0
	SOA <sub>TR</sub>	Krakow	0.45	0.0

		Milan	0.42	0.0
		Paris	0.46	0.0
		Zurich	0.60	0.0

846

847 **Table 3. Toy experiment statistics of (a) Factorisation performance. (b) Comparison to truth. Green**  
848 **sequential colorscales represent variables whose larger value leans to a better performance and the blue-**  
849 **to-red divergent colorscales (centered at 1, in white) represent  $G/G_0$  divergence with respect to 1. Red bars**  
850 **in (a) depict deviations from the ideal 0 value.**

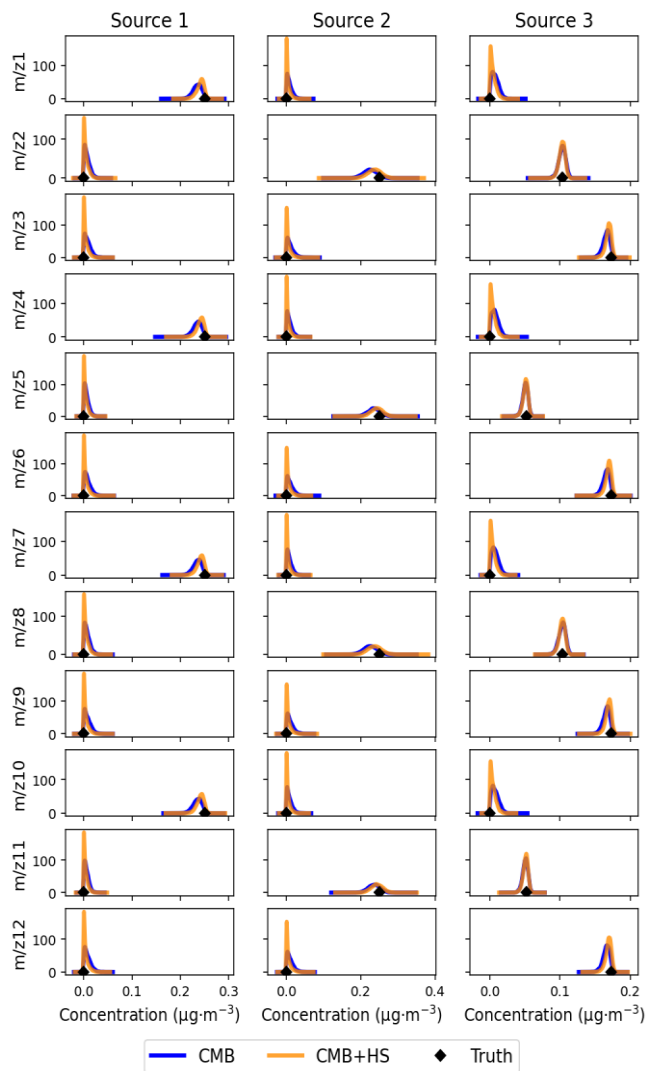
851

(a)

Model	Factorisation		
	R <sup>2</sup>	Median( Z-X /sigma)	Max( Z-X /sigma)
CMB	0.9985	0.2542	0.5755
CMB+HS	0.9996	0.2648	0.4774
PMF	0.9979	0.2658	0.5847
BMF	0.9650	0.2125	1.2917
BMF+HS	0.9689	0.2107	1.2863
BAMF	0.9818	0.1222	0.7247
BAMF+HS	0.9820	0.1208	0.7180
BAMF-ARI	0.9806	0.0947	1.0257
BAMF-ARI+HS	0.9790	0.1171	1.0297
BMF-GS	0.9657	0.2024	1.3031
BAMF-GS	0.9818	0.1576	0.9082

(b)

Model	Sources	G				F		
		G/G <sub>0</sub>	R <sup>2</sup>	$\rho$	R <sup>2</sup>	Gini	Gini ratio	Zeros sum
CMB	Source1	1.00	1.00	0.82	1.00	0.61	0.91	0.06
	Source2	1.00	1.00	0.82	1.00	0.60	0.90	0.08
	Source3	1.00	1.00	0.96	1.00	0.44	0.92	0.03
CMB+HS	Source1	1.00	1.00	0.82	1.00	0.63	0.95	0.03
	Source2	1.00	1.00	0.82	1.00	0.63	0.95	0.04
	Source3	1.00	1.00	0.96	1.00	0.47	0.96	0.02
PMF	Source1	1.00	0.96	0.82	0.95	0.35	0.52	0.36
	Source2	3.29	0.97	0.82	0.88	0.30	0.45	0.42
	Source3	0.65	0.74	0.79	0.81	0.31	0.64	0.2
BMF	Source1	1.08	0.87	0.82	0.76	0.25	0.37	0.48
	Source2	4.10	0.84	0.51	0.43	0.16	0.23	0.58
	Source3	0.60	0.46	0.79	0.80	0.21	0.44	0.25
BMF+HS	Source1	1.11	0.88	0.82	0.77	0.25	0.38	0.48
	Source2	3.92	0.85	0.82	0.50	0.15	0.23	0.57
	Source3	0.60	0.44	0.79	0.84	0.22	0.46	0.23
BAMF	Source1	1.66	0.98	0.82	0.78	0.27	0.41	0.46
	Source2	1.99	0.95	0.82	0.97	0.33	0.50	0.37
	Source3	0.54	0.50	0.96	1.00	0.38	0.79	0.08
BAMF+HS	Source1	1.96	0.98	0.82	0.76	0.27	0.40	0.47
	Source2	1.28	0.95	0.82	0.99	0.58	0.86	0.11
	Source3	0.51	0.48	0.96	1.00	0.44	0.93	0.02
BAMF-ARI	Source1	1.70	0.98	0.82	0.79	0.27	0.41	0.46
	Source2	3.05	0.92	0.82	0.89	0.37	0.55	0.36
	Source3	0.42	0.50	0.96	0.94	0.43	0.90	0.08
BAMF-ARI+HS	Source1	1.92	0.99	0.82	0.77	0.26	0.39	0.46
	Source2	2.58	0.89	0.82	0.90	0.48	0.72	0.36
	Source3	0.38	0.49	0.96	0.97	0.49	1.03	0.08
BMF-GS	Source1	0.88	0.92	0.82	0.63	0.21	0.31	0.52
	Source2	1.12	0.86	0.82	0.71	0.20	0.30	0.53
	Source3	1.02	0.29	0.79	0.91	0.22	0.46	0.22
BAMF-GS	Source1	0.89	0.94	0.82	0.66	0.21	0.32	0.53
	Source2	1.12	0.95	0.82	0.70	0.19	0.28	0.53
	Source3	1.02	0.36	0.79	0.90	0.22	0.46	0.22
BAMF-Lasso	Source1	1.76	0.98	0.82	0.76	0.27	0.40	0.47
	Source2	2.02	0.95	0.82	0.95	0.34	0.50	0.37
	Source3	0.49	0.47	0.96	1.00	0.41	0.86	0.05
BAMF-Spike-Slab	Source1	1.57	0.97	0.82	0.77	0.26	0.40	0.47
	Source2	1.78	0.95	0.82	0.99	0.34	0.52	0.34
	Source3	0.62	0.50	0.96	0.98	0.33	0.69	0.12

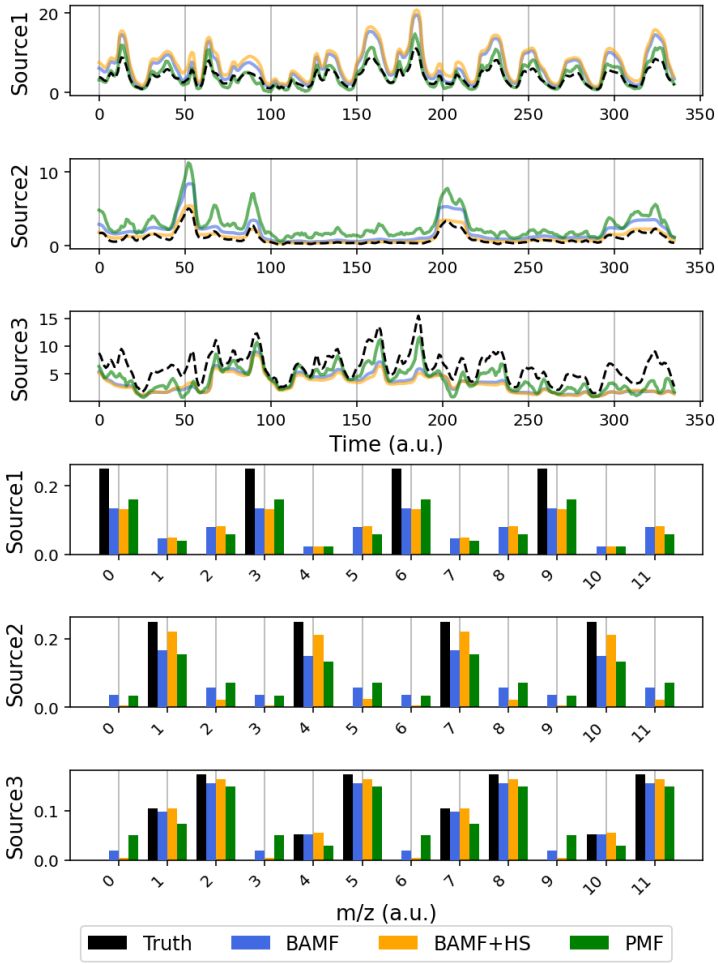


853

854

**Figure 1. F matrix components distributions for CMB and CMB+HS (solid lines) compared to truth (markers).**

855

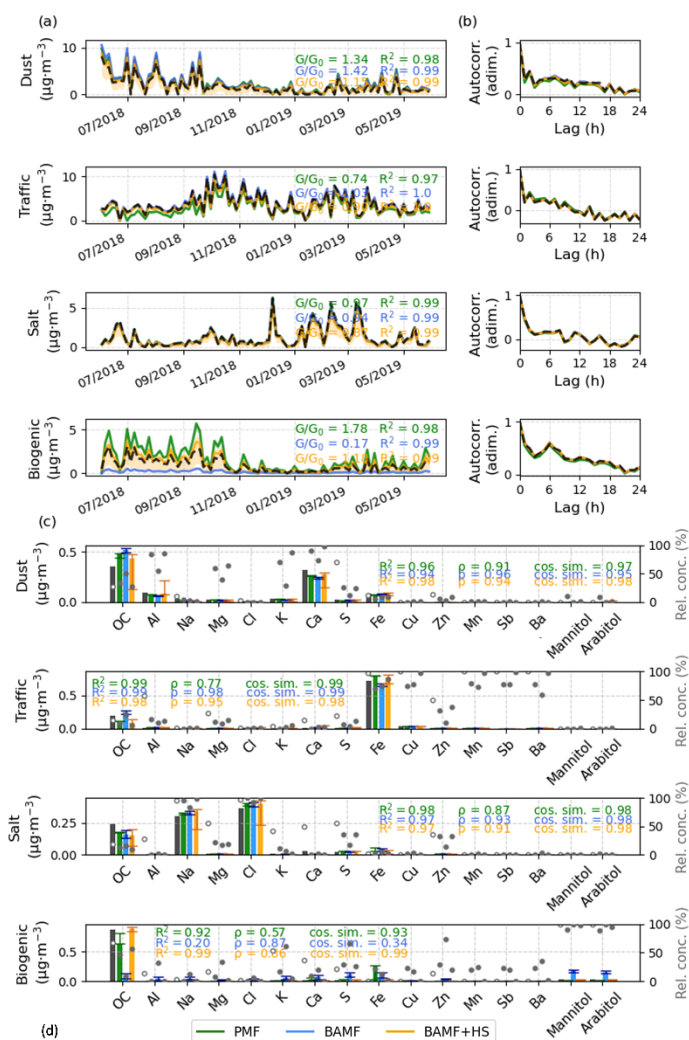


856

857

858

**Figure 2. Source apportionment results for the toy dataset obtained using PMF, BAMF, and BAMF+HS, compared against the true solution (black bars). (a) Factor time series. (b) Factor profiles.**

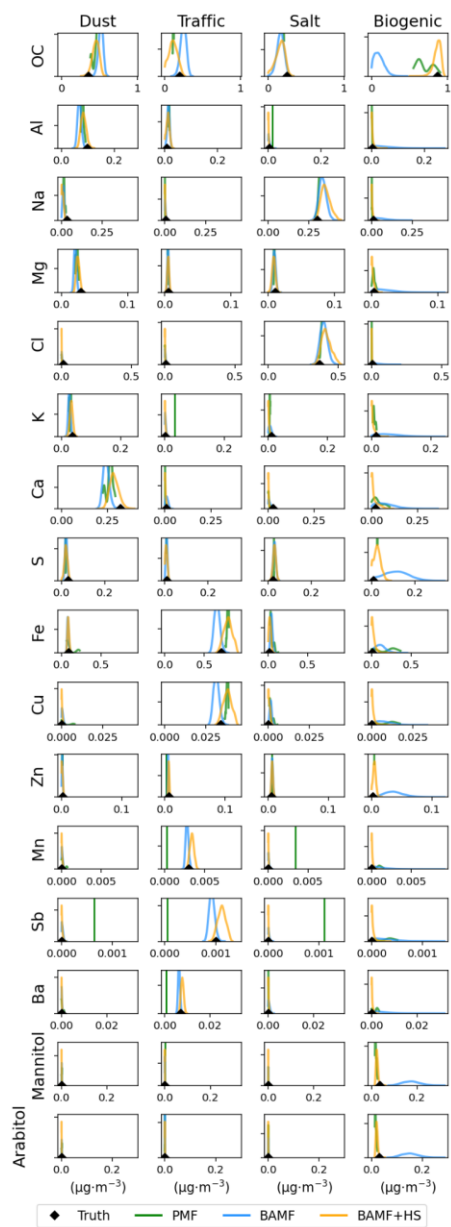


Factor	Model	F contr. R <sup>2</sup>	F contr. ρ	F Gini	F Gini ratio (*)	Truth zeros sum
Dust	PMF	0.95	0.84	0.79	0.90	0.0035
	BAMF	0.77	0.90	0.80	1.08	0.0025
	BAMF-HS	0.94	0.90	0.79	1.07	0.0011
Traffic	PMF	0.99	0.90	0.89	1.19	0.0000
	BAMF	0.93	0.94	0.85	0.99	0.0005
	BAMF-HS	0.995	0.93	0.88	1.02	0.0004
Salt	PMF	0.95	0.84	0.79	0.90	0.0012
	BAMF	0.95	0.88	0.80	1.01	0.0118
	BAMF HS	0.98	0.87	0.82	1.04	0.0031
Biogenic	PMF	0.87	0.43	0.85	1.08	0.0035
	BAMF	0.53	0.51	0.50	0.56	0.0118
	BAMF-HS	0.96	0.84	0.90	1.01	0.0007
Σλ (*)	PMF	3.80	3.04	3.34	0.43	0.0198
	BAMF	3.18	3.23	2.95	0.53	0.0172
	BAMF HS	<b>3.88</b>	<b>3.54</b>	<b>3.39</b>	0.15	<b>0.0031</b>

859

860 **Figure 3. Synthetic offline dataset source apportionment results for PMF, BAMF, and BAMF+HS models. (a) Time**  
 861 **Series. (b) Autocorrelation. (c) Profiles. (d) Table with additional metrics for comparison to truth. Bold numbers reflect**  
 862 **the highest value amongst models. F contr. represents here the percentage of each factor into a given species. The sum**  
 863 **row reflects the overall performance of the model for all sources for each statistic metric except for the ones marked**  
 864 **with (\*), in which the difference to 1 in absolute value is summed up.**

865



866

867

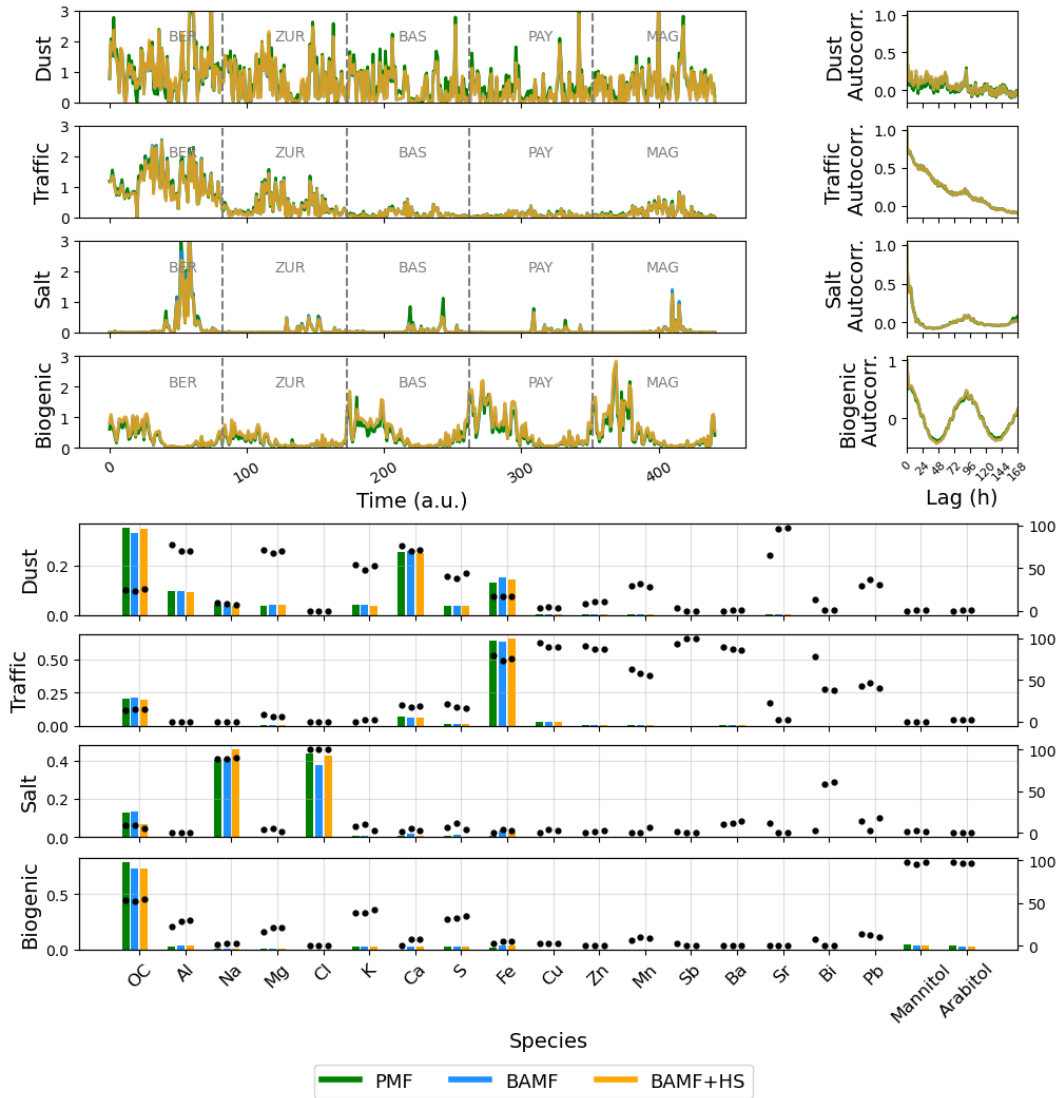
**Figure 4. Profile components distribution for PMF, BAMF, BAMF+HS (solid colored lines) in comparison to the truth (markers) on the real-world filters dataset. Rows represent the species of the source apportionment and columns represent sources.**

868

869

870

871



872

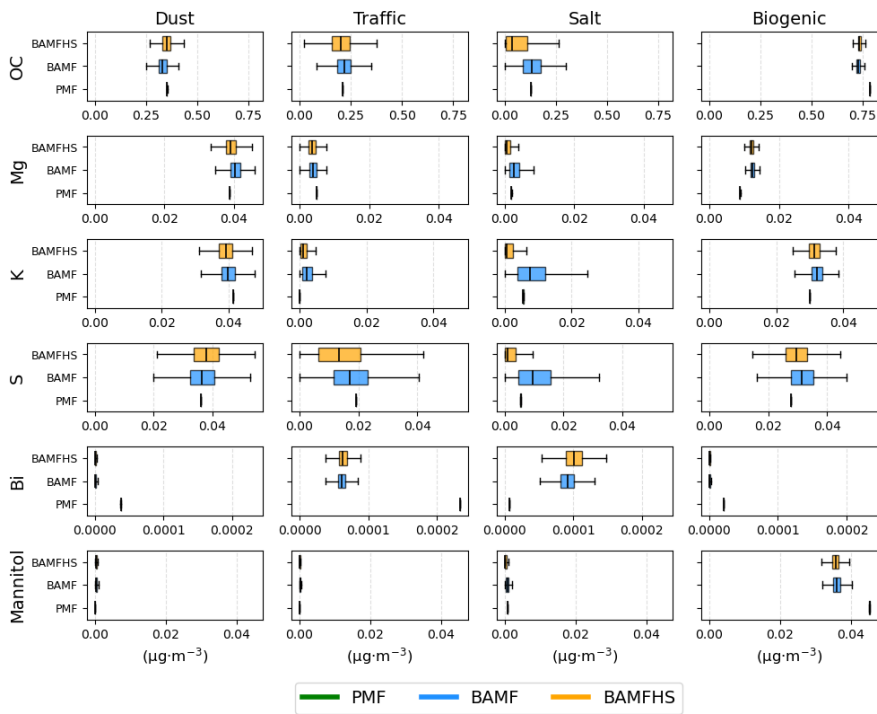
873 **Figure 5. Comparison of PMF, BAMF, BAMF+HS for the real-world filters dataset. From left to right and**  
 874 **top to bottom: time series, autocorrelation, and profile plots. The dots in the profiles (right axis) show the**  
 875 **contribution of each species to the source.**

876 **Table 4. Offline real-world dataset reconstruction and sparsity statistics. Bold numbers reflect the highest**  
 877 **value amongst models.**

Model	$R^2(Z, X)$	Median $ X-Z /\sigma$	Median $ X-Z /\sigma$	Factor	F Gini
<b>PMF</b>	0.68	0.77	10.52	Dust	<b>0.77</b>
				Traffic	<b>0.87</b>
				Salt	0.86
				Biogenic	<b>0.87</b>
<b>BAMF</b>	0.67	0.75	11.13	Dust	0.76

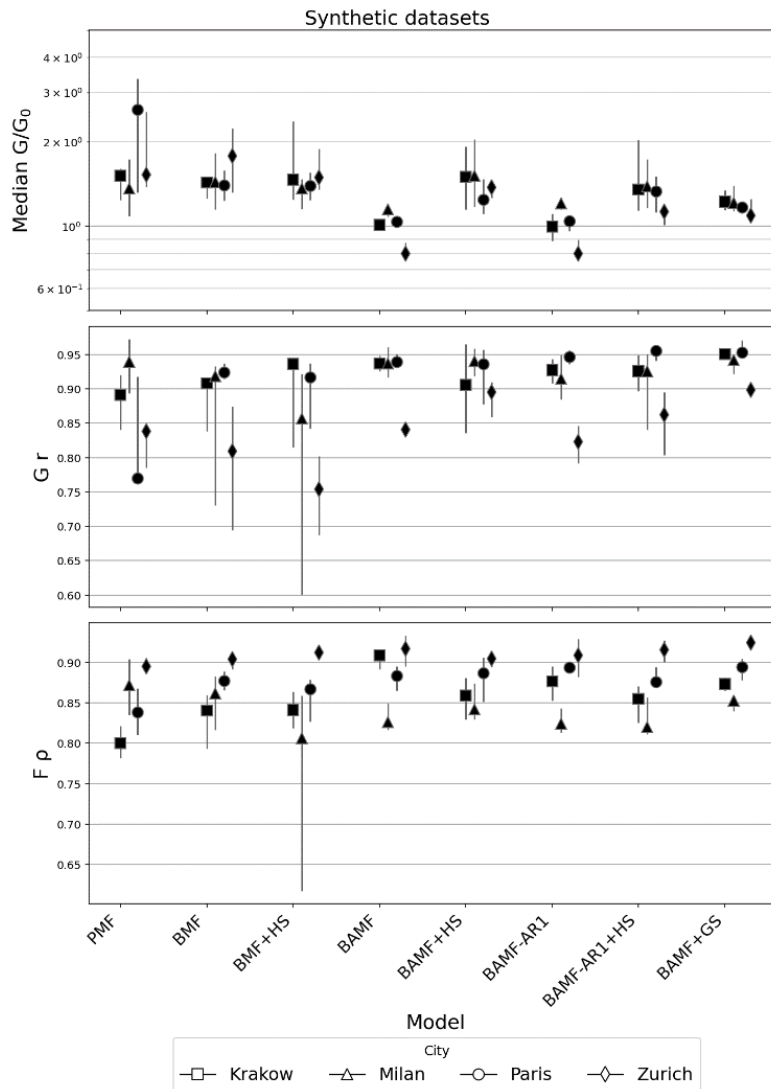
				Traffic	<b>0.87</b>
				Salt	0.84
				Biogenic	0.83
<b>BAMF+HS</b>	0.67	0.75	11.12	Dust	<b>0.77</b>
				Traffic	<b>0.87</b>
				Salt	<b>0.87</b>
				Biogenic	0.83

878  
879  
880  
881  
882



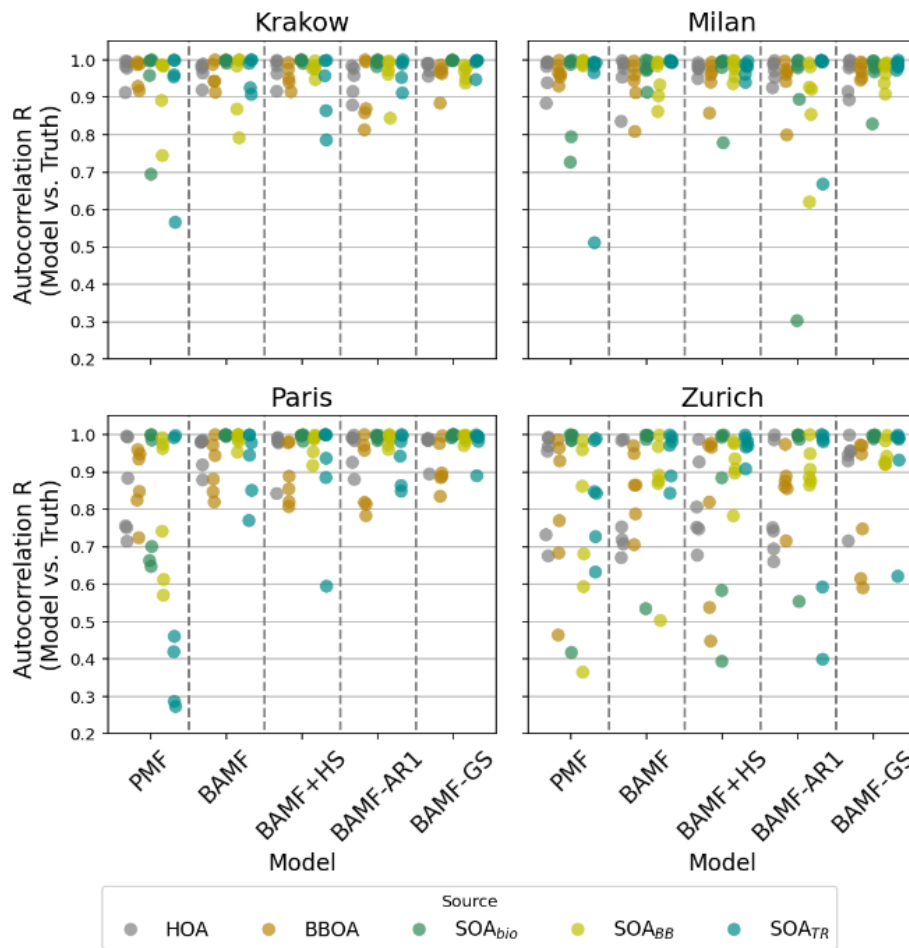
883  
884  
885  
886

**Figure 6. Boxplot distributions of individual profile components derived from PMF, BAMF, and BAMF+HS analyses for the real-world filter dataset. A complete comparison of all profiles is presented in Figure S9.**



887

888 **Figure 7. European cities synthetic datasets summary statistics; from top to bottom, median ratio time series with truth**  
 889 **( $G/G_0$ ), Pearson correlation coefficient of  $G$  with truth ( $G r$ ), Spearman correlation coefficient of  $F$  with truth ( $F \rho$ ).**  
 890 **The axis of the  $G/G_0$  plot is in logarithmic scale.**

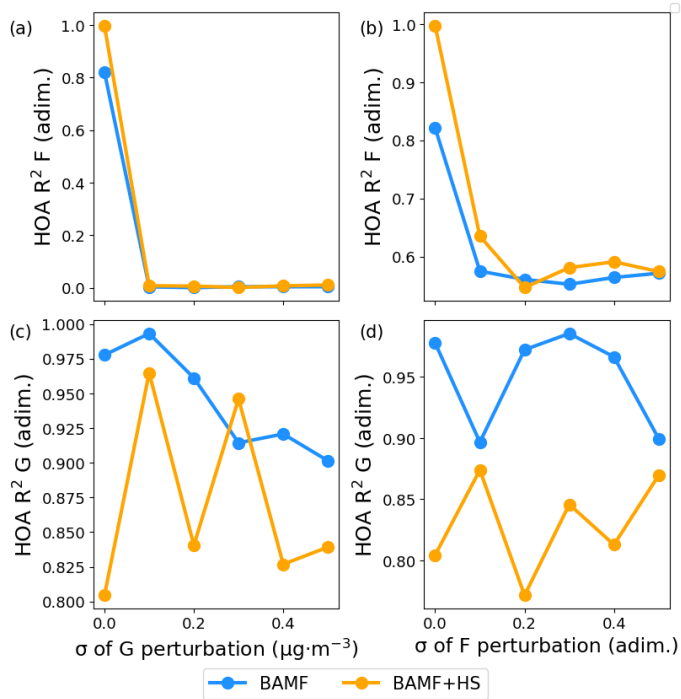


891

892 **Figure 8. Pearson correlation of the autocorrelations of model solutions with the truth for all factors and all cities.**

893

894



895

896

897

**Figure 9. Squared Pearson coefficient of F, G matrix with original truth F, G matrices of the BAMF, BAMF+HS models with the degrees of perturbation in F and G.**

898